

## Active superelasticity in three-dimensional epithelia of controlled shape

Ernest Latorre<sup>1,2</sup>, Sohan Kale<sup>2</sup>, Laura Casares<sup>1</sup>, Manuel Gómez-González<sup>1</sup>, Marina Uroz<sup>1</sup>, Léo Valon<sup>1</sup>, Roshna V. Nair<sup>3</sup>, Elena Garreta<sup>1</sup>, Nuria Montserrat<sup>1,4</sup>, Aránzazu del Campo<sup>3,5</sup>, Benoit Ladoux<sup>6,7</sup>, Marino Arroyo<sup>1,2\*</sup> & Xavier Trepat<sup>1,4,8,9\*</sup>

<sup>1</sup>Institute for Bioengineering of Catalonia (IBEC), The Barcelona Institute for Science and Technology (BIST), Barcelona, Spain.

<sup>2</sup>LaCàN, Universitat Politècnica de Catalunya-BarcelonaTech, Barcelona, Spain.

<sup>3</sup>INM-Leibniz Institut für Neue Materialien, Saarbrücken, Germany.

<sup>4</sup>Centro de Investigación Biomédica en Red en Bioingeniería, Biomateriales y Nanomedicina, Barcelona, Spain.

<sup>5</sup>Chemistry Department, Saarland University, Saarbrücken, Germany.

<sup>6</sup>CNRS UMR 7592, Institut Jacques Monod (IJM), Université Paris Diderot, Paris, France.

<sup>7</sup>Mechanobiology Institute (MBI), National University of Singapore, Singapore, Singapore.

<sup>8</sup>Unitat de Biofísica i Bioenginyeria, Universitat de Barcelona, Barcelona, Spain.

<sup>9</sup>Institució Catalana de Recerca i Estudis Avançats (ICREA), Barcelona, Spain.

\*email: marino.arroyo@upc.edu; xtrepata@ibecbarcelona.eu

**Fundamental biological processes are carried out by curved epithelial sheets that enclose a pressurized lumen. How these sheets develop and withstand three-dimensional deformations has remained unclear. Here we combine measurements of epithelial tension and shape with theoretical modelling to show that epithelial sheets are active superelastic materials. We produce arrays of epithelial domes with controlled geometry. Quantification of luminal pressure and epithelial tension reveals a tensional plateau over several-fold areal strains. These extreme tissue strains are accommodated by highly heterogeneous cellular strains, in seeming contradiction to the measured tensional uniformity. This phenomenon is reminiscent of superelasticity, which is a behaviour that is generally attributed to microscopic material instabilities in metal alloys. We show that in epithelial cells this instability is triggered by a stretch-induced dilution of the actin cortex, and is rescued by the intermediate filament network. Our study unveils a type of mechanical behaviour—which we term active superelasticity—that enables epithelial sheets to sustain extreme stretching under constant tension.**

Epithelial tissues enable key physiological functions, including morphogenesis, transport, secretion and absorption<sup>1</sup>. To perform these functions, epithelia often adopt a three-dimensional (3D) architecture that consist of a curved cellular sheet enclosing a pressurized fluid-filled lumen<sup>2,3</sup>. The loss of this 3D architecture is associated with developmental defects, inflammatory conditions and cancer<sup>4,5</sup>.

The acquisition of a 3D shape by epithelial sheets requires a tight control of cellular deformation, mechanical stress and luminal pressure. How these mechanical variables are tuned together to sculpt 3D epithelia is unknown, because current techniques to map epithelial mechanics are largely restricted to two-dimensional (2D) layers seeded on a flat substrate<sup>6,7</sup> or freely standing between cantilevers<sup>5</sup>. Here we report direct measurements of traction, tension, pressure and deformation in 3D epithelial monolayers of controlled size and shape. These measurements establish that epithelial monolayers exhibit active superelasticity, an unanticipated mechanical behaviour that enables extreme deformations at nearly constant tension.

### **Micropatterned epithelial domes**

We used transmural pressure as the morphogenetic driving force to shape epithelial monolayers in 3D. We seeded Madin-Darby canine kidney (MDCK) cells on a soft polydimethylsiloxane (PDMS) substrate that was homogeneously coated with fibronectin except for micropatterned, non-adhesive areas of precise geometry (Fig. 1a). A few hours after seeding cells covered the adherent regions of the gel, and with time they invaded the non-adherent areas<sup>8,9</sup>. Because MDCK cells are known to actively pump osmolites in the apico-basal direction<sup>10,11</sup>, we reasoned that fluid pressure should build up in the interstitial space between cells and the impermeable substrate, which would lead to tissue delamination from the substrate in the non-adherent regions. Consistent with this rationale, we observed the spontaneous formation of multicellular epithelial domes that closely followed micropatterned shapes, such as circles, rectangles and stars (Fig. 1b–e, Extended Data Fig. 1a–d). In contrast to spontaneous doming by delamination<sup>10,11</sup>, our control of the dome footprint gave us access to large variations in the aspect ratio of the dome (Fig. 1c–e).

### **Measurement of dome mechanics**

To measure dome mechanics, we focused on circular patterns and implemented 3D traction microscopy to determine the three components of tractions at the surface of the PDMS substrate (Fig. 2a, b). Traction in adherent regions showed large fluctuations without a clear spatial

pattern (Fig. 2b). By contrast, non-adherent areas exhibited systematic normal and nearly uniform negative tractions that indented the substrate. In a narrow annular region at the margin of the dome footprint, the traction vector consistently exhibited a positive normal component that pulled the substrate upward. These observations—along with the morphology of the domes—established that the lumen was in a state of hydrostatic pressure, and that the free-standing part of the monolayer sustained tension to balance this pressure (Fig. 2a).

We then wondered whether we could map the tensional state of the dome, even though constituent cells did not directly generate tractions on the substrate. Epithelial domes followed a spherical cap geometry very closely (Fig. 2b), which implies that their surface tension ( $\sigma$ ) was isotropic, uniform and obeyed Laplace's law ( $2\sigma = R \times \Delta P$ , in which  $\Delta P$  is the transmural pressure and  $R$  the radius of curvature of the dome; see Supplementary Note 1). This equation enabled us to measure the epithelial tension of the domes, as the normal traction in the non-adherent regions provides a direct readout of  $\Delta P$  and  $R$  could be measured from confocal stacks. We found tissue tensions in the millinewton per metre range, similar to previous measurements in 2D monolayers<sup>5,7</sup>.

To test the principle behind our tension measurement, we perturbed the system with the Rho kinase inhibitor Y-27632, which is known to reduce tissue tension. Because the epithelial barrier has finite permeability to water, the enclosed volume—and hence  $R$ —cannot change instantaneously upon this perturbation. Consequently, Laplace's law requires tension relaxation be paralleled by a pressure drop. This prediction was confirmed by our measurements (Fig. 2c–g, Extended Data Fig. 2a–c, Supplementary Video 1). We also examined water transport by subjecting domes to hyper-osmotic shocks (Supplementary Note 2). Volume dynamics under osmotic perturbations were consistent with a simple physical picture, in which the epithelium behaves in a manner similar to a semi-permeable membrane actively pumping osmolites at nearly constant rate.

### **Constitutive relation between dome tension and strain**

In the absence of pharmacological or osmotic perturbations and over timescales of hours, epithelial domes exhibited large volume fluctuations (Fig. 3a, Supplementary Video 2). These fluctuations involved periods of slow swelling and de-swelling combined with sudden volume drops, often up to total dome collapse and subsequent rebirth. The magnitude of collapse events, presumably caused by localized disruptions of epithelial integrity, and the duration of swelling

phases exhibited high variability (Fig. 3a, b, Extended Data Fig. 3). During these spontaneous fluctuations, we tracked luminal pressure and dome geometry, which provided a measurement of epithelial tension at different degrees of swelling (Fig. 3c–e, Supplementary Video 2). To examine these data, we represented tension in the free-standing tissue as a function of nominal areal strain of the dome  $\varepsilon_d = (h/a)$ , which is defined as the difference between the actual area of the dome  $\pi(h^2 + a^2)$  and the area of the non-adhesive region  $\pi a^2$ , normalized by the latter (see Fig. 2b for a definition of  $h$  and  $a$ ). All domes exhibited tensions of about  $1 \text{ mN m}^{-1}$  at small strains. At moderate strains (below 100%), tension progressively increased according to a highly reproducible law. Beyond this point, tension exhibited larger scatter but reached a plateau at about  $2 \text{ mN m}^{-1}$  for areal strains up to 300% (Fig. 3e, Extended Data Fig. 4a). The existence of this plateau is notable, as it reveals that epithelial domes maintain tensional homeostasis while undergoing deformations that change their area by up to fourfold. Human epithelial colorectal adenocarcinoma (Caco-2) cells showed a plateau at similar tension but lower strain (Extended Data Fig. 4b, c; see Supplementary Table 1 for a list of cell lines known to form domes).

A number of mechanisms could contribute to such tensional homeostasis, including directed<sup>12</sup> or accelerated<sup>13</sup> cell division, junctional network rearrangements<sup>14</sup>, and cell exchange between domes and the adjacent adhered tissue. Visual examination of the domes showed that cell division and extrusion were rare (Supplementary Videos 3, 4). Moreover, the number of cells in the dome remained constant during the several-fold increases in dome area (Extended Data Fig. 1f). We thus concluded that the tension–strain response of the tissue had to depend on the mechanics of cell stretching.

To understand the strain–tension relation of the dome monolayer, we developed a theoretical vertex model in 3D<sup>15,16</sup>. The model is based on the well-established observation that the major determinant of epithelial-cell mechanics is the actin cortex<sup>17</sup>. In the time-scales of our experiments, this thin cytoskeletal network behaves in a manner similar to a fluid gel, and is capable of developing contractile tension owing to myosin motors<sup>17</sup>. In 3D vertex models, these active tensions act along lateral ( $\gamma$ ) and apico-basal ( $\gamma_{ab}$ ) faces of polyhedral cells (Fig. 3g, Supplementary Note 3). Assuming constant cell volume<sup>5</sup> and idealizing cells as regular hexagonal prisms of uniform thickness under uniform equibiaxial strain, this model predicts that the effective surface tension of the tissue depends on cellular areal strain,  $\varepsilon_c$ , as

$$\sigma = \gamma_{ab} - k \frac{\gamma_1}{(1 + \varepsilon_c)^{3/2}} \quad (1)$$

in which  $k$  is a non-dimensional constant. This active constitutive relation recapitulates the initial increase in tension and the subsequent plateau at larger areal strain that are observed experimentally (Fig. 3e, f). The tendency of tension to plateau at large strains emerges naturally from the fact that the area of lateral faces decreases with cell stretching and, hence, tissue tension converges to apico-basal tension. To theoretically examine tissue stretching by dome swelling, we developed a computational version of the vertex model shown in Fig. 3g (Supplementary Note 3). The tension–strain law evaluated using this computational approach closely matched the analytical constitutive relation in equation (1) (Fig. 3f).

Although this simple theoretical framework captured the tension–strain relationship, it missed a notable experimental feature: during swelling and de-swelling, we systematically observed cells that barely changed area coexisting with cells that reached cellular areal strains of up to 1,000%, which is five times greater than the average dome strain (Fig. 4a, b, Extended Data Fig. 5a–e, Supplementary Videos 5, 6 and 7). This extreme heterogeneity in strain is reminiscent of that observed in highly stretched epithelia *in vivo*, such as the trophoblast in human and mouse blastocysts<sup>18,19</sup> (Extended Data Fig. 5f, g). In both epithelial domes and blastocysts, strain heterogeneity would seem to be in contradiction with their spherical shape, which implies tensional uniformity. The heterogeneity of cellular strain increased sharply beyond areal strains of approximately 100% (Fig. 4a, Extended Data Fig. 5). This strain threshold coincides with the onset of the tensional plateau and with the increase in the scatter of tissue tension (Fig. 3e).

### **Epithelial domes exhibit superelastic behaviour**

Taken together, our experiments show that epithelial domes exhibit large reversible deformations and a tensional plateau during which superstretched constitutive elements coexist with barely stretched ones. These uncommon material features are defining hallmarks of superelasticity, a behaviour that is observed in some inert materials such as nickel–titanium alloys<sup>20</sup>. These materials are able to undergo large and reversible deformations at constant stress by heterogeneously switching between low- and high-strain phases<sup>20</sup>. The microscopic trigger of superelasticity is a mechanical instability that results from a decreasing branch in the stress–strain relation of the material (strain softening). We reasoned that, by analogy with this behaviour, cell monolayers might behave as superelastic materials by switching from barely

stretched to superstretched cellular states at constant tension. To explore this possibility further, we sought a strain-softening mechanism that would explain the mechanical instability that underlies the transition between low and high-strain phases.

Because cellular deformations increased the surface area of the actin cortex by over threefold, we hypothesized that strain softening arose from the limited availability of cytoskeletal components<sup>21</sup>. Scarcity of cytoskeletal components could lead to stretch-induced cortical dilution, which could impair the ability of the cortex to generate active tension<sup>22</sup> (Supplementary Note 3). To test this hypothesis, we incorporated cortical dynamics in the 3D vertex model. We focused on actin as the main cortical component, although cortical depletion could also affect actin cross-linkers, polymerization agents and molecular motors. In our model, cortical thickness—or, equivalently, cortical surface density  $\rho$ —is determined by a balance between polymerization at the plasma membrane and depolymerization in the bulk of the actin gel<sup>23</sup>. If the availability of cytoskeleton components ready for polymerization is infinite, this model predicts that cortical density  $\rho$ , and hence cortical tension  $\gamma$ , are constant and independent of strain, which leads to equation (1). However, if free cytoskeleton components are limited, the model predicts a progressive depletion of cortical density  $\rho$  with cellular areal strain—and hence strain softening when the cortex becomes sufficiently thin<sup>22</sup> (Fig. 4c). To test this physical mechanism, we measured cortical surface density  $\rho$  in cells located at the apex of fixed domes and represented this surface density as function of cell strain  $\varepsilon_c$ . These experiments showed that superstretched cells systematically exhibited less-dense cortices (Fig. 4d–g, Extended Data Fig. 6). Moreover, live imaging of cells labelled with SiR–actin showed that the actin cortex became progressively and reversibly diluted with cell stretching (Fig. 4h–j, Supplementary Video 8).

We exogenously interfered with cell–cell junctions and the actin cytoskeleton (Extended Data Figs. 2, 7). Notably, we locally triggered actin depolymerization using a photoactivatable derivative of cytochalasin D. Upon activation, targeted cells increased their area without noticeable changes in the overall shape of the dome (Extended Data Fig. 8, Supplementary Video 9), which indicates that cortical dilution is sufficient to cause large increases in cell area. Taken together, these results are consistent with our hypothesis that cortical dilution underlies cellular superstretching.

Besides strain softening, superelasticity also requires re-stiffening at large strains to confine the high-strain phase. Without such a mechanism, the first cell to reach the softening

regime would easily deform further, relaxing neighbouring cells and eventually localizing deformation in an unbounded fashion<sup>24</sup> (Supplementary Note 3, Supplementary Video 10). Multiple mechanisms could stiffen cells that are subjected to extreme stretching, including exhaustion of the plasma membrane reservoir<sup>25</sup>, crowding of adhesion molecules in shrinking cell–cell adhesions<sup>26</sup>, confinement of the nucleus between tensed cortices or load transfer to the otherwise-relaxed intermediate filament cytoskeleton<sup>5</sup>. Our experiments do not rule out any of these possibilities but do provide support for the last. Indeed, intermediate filaments in superstretched cells appeared unusually straight, which suggests these filaments are load-bearing (Fig. 4l–n, Extended Data Fig. 9). To further test this mechanism, we laser-ablated keratin-18 filaments. In weakly stretched cells, laser ablation did not induce changes in cell area. By contrast, laser ablation in superstretched cells resulted in a rapid increase in cell area, indicating that intermediate filaments in superstretched cells—but not in relaxed cells—bear tension (Fig. 4o, p, Extended Data Fig. 10). By introducing re-stiffening at large strains into our computational vertex model, we were able to recapitulate our most-salient experimental observations (Supplementary Videos 11, 12). At low levels of dome stretching, tissue tension increased with strain, and heterogeneity in cellular strain was low (Fig. 4k, q, r). By contrast, at high levels of stretching, the domes reached a tensional plateau and heterogeneity in cellular strain rose sharply. Thus, strain softening by stretch-induced depletion of cortical components followed by re-stiffening at extreme stretches configures an effective bistable energy landscape of active origin that explains the emergence of a stable high-strain phase of superstretched cells under sufficiently large tension (Fig. 4r, Supplementary Note 3).

Active superelasticity provides a mechanism for epithelial tissues to undergo extreme and reversible deformations at nearly constant tension by progressive switching of individual cells to a superstretched state. Our study suggests that, because the underlying subcellular mechanisms are generic, superelasticity may have a broad applicability *in vivo*. For example, epithelial superelasticity may mediate the spreading of superstretched extra-embryonic tissues and their subsequent rapid compaction<sup>27</sup>. Active superelasticity may also enable extreme cellular strains in the trophectoderm during the swelling and hatching of mammalian blastocysts<sup>18,19</sup>. Besides providing a framework to understand epithelial mechanics and morphogenesis *in vivo*, the material laws established here set the stage for a rational manipulation of cell monolayers in organoids and organ-on-a-chip technologies<sup>28</sup>.

**Online content** Any methods, additional references, Nature Research reporting summaries, source data, statements of data availability and associated accession codes are available at

Received 13 November 2017; accepted 8 October 2018

1. Alberts, B., Wilson, J. & Hunt, T. *Molecular Biology of the Cell*, 6th edn, (Garland Science, New York, 2014).
2. Bosveld, F. et al. Mechanical control of morphogenesis by Fat/Dachsous/Four-jointed planar cell polarity pathway. *Science* **336**, 724–727 (2012).
3. He, B., Dubrovinski, K., Polyakov, O. & Wieschaus, E. Apical constriction drives tissue-scale hydrodynamic flow to mediate cell elongation. *Nature* **508**, 392–396 (2014).
4. Wilson, P. D. Polycystic kidney disease. *N. Engl. J. Med.* **350**, 151–164 (2004).
5. Harris, A. R. et al. Characterizing the mechanics of cultured cell monolayers. *Proc. Natl Acad. Sci. USA* **109**, 16449–16454 (2012).
6. Tambe, D. T. et al. Collective cell guidance by cooperative intercellular forces. *Nat. Mater.* **10**, 469–475 (2011).
7. Vincent, R. et al. Active tensile modulus of an epithelial monolayer. *Phys. Rev. Lett.* **115**, 248103 (2015).
8. Vedula, S. R. et al. Mechanics of epithelial closure over non-adherent environments. *Nat. Commun.* **6**, 6111 (2015).
9. Nier, V. et al. Tissue fusion over nonadhering surfaces. *Proc. Natl Acad. Sci. USA* **112**, 9546–9551 (2015).
10. Leighton, J., Brada, Z., Estes, L. W. & Justh, G. Secretory activity and oncogenicity of a cell line (MDCK) derived from canine kidney. *Science* **163**, 472–473 (1969).
11. Tanner, C., Frambach, D. A. & Misfeldt, D. S. Transepithelial transport in cell culture. A theoretical and experimental analysis of the biophysical properties of domes. *Biophys. J.* **43**, 183–190 (1983).
12. Wyatt, T. P. et al. Emergence of homeostatic epithelial packing and stress dissipation through divisions oriented along the long cell axis. *Proc. Natl Acad. Sci. USA* **112**, 5726–5731 (2015).



13. Gudipaty, S. A. et al. Mechanical stretch triggers rapid epithelial cell division through Piezo1. *Nature* **543**, 118–121 (2017).
14. Guillot, C. & Lecuit, T. Mechanics of epithelial tissue homeostasis and morphogenesis. *Science* **340**, 1185–1189 (2013).
15. Alt, S., Ganguly, P. & Salbreux, G. Vertex models: from cell mechanics to tissue morphogenesis. *Phil. Trans. R. Soc. Lond. B* **372**, 20150520 (2017).
16. Hannezo, E., Prost, J. & Joanny, J. F. Theory of epithelial sheet morphology in three dimensions. *Proc. Natl Acad. Sci. USA* **111**, 27–32 (2014).
17. Salbreux, G., Charras, G. & Paluch, E. Actin cortex mechanics and cellular morphogenesis. *Trends Cell Biol.* **22**, 536–545 (2012).
18. Hildebrand, S. et al. The E-cadherin/AmotL2 complex organizes actin filaments required for epithelial hexagonal packing and blastocyst hatching. *Sci. Rep.* **7**, 9540 (2017).
19. Deglincerti, A. et al. Self-organization of the *in vitro* attached human embryo. *Nature* **533**, 251–254 (2016).
20. Otsuka, K. & Wayman, C. M. *Shape Memory Materials* (Cambridge Univ. Press, Cambridge, 1998).
21. Suarez, C. & Kovar, D. R. Internetwork competition for monomers governs actin cytoskeleton organization. *Nat. Rev. Mol. Cell Biol.* **17**, 799–810 (2016).
22. Chugh, P. et al. Actin cortex architecture regulates cell surface tension. *Nat. Cell Biol.* **19**, 689–697 (2017).
23. Turlier, H., Audoly, B., Prost, J. & Joanny, J. F. Furrow constriction in animal cell cytokinesis. *Biophys. J.* **106**, 114–123 (2014).
24. Jirásek, M. & Bazant, Z. P. *Inelastic Analysis of Structures* (Wiley, West Sussex, England, 2002).
25. Raucher, D. & Sheetz, M. P. Characteristics of a membrane reservoir buffering membrane tension. *Biophys. J.* **77**, 1992–2002 (1999).
26. Maître, J. L. & Heisenberg, C. P. Three functions of cadherins in cell adhesion. *Curr. Biol.* **23**, R626–R633 (2013).

27. Hilbrant, M., Horn, T., Koelzer, S. & Panfilio, K. A. The beetle amnion and serosa functionally interact as apposed epithelia. *eLife* **5**, e13834 (2016).
28. Clevers, H. Modeling development and disease with organoids. *Cell* **165**, 1586–1597 (2016).

**Acknowledgements** We thank N. Castro for technical assistance; C. Pérez-González, A. Labernadie, R. Sunyer and A. Torres-Sánchez for discussions and G. Charras for providing cells; J. Colombelli, L. Bardia and A. Lladó (IRB) for assistance with laser ablation and photoactivation; N. Borges from Embryotools S.L. for fixation of mouse blastocysts. This work was supported by the Spanish Ministry of Economy and Competitiveness/FEDER (BFU2015-65074-P to X.T., DPI2015-71789-R to M.A., SAF2017-89782-R to NM, SAF2015-72617-EXP to N.M., RYC-2014-16242 to N.M.), the Generalitat de Catalunya and CERCA program (2014-SGR-927 to X.T., 2017-FI-B1-00068 grant to E.L., 2014-SGR-1471 to M.A., 2017 SGR 1306 to N.M., ‘ICREA Academia’ award to M.A.), the European Research Council (CoG-616480 to X.T., CoG-681434 to M.A., CoG-617233 to B.L., StG-640525 to N.M.), European Commission (project H2020-FETPROACT-01-2016-731957 to M.A., A.d.C. and X.T.), LABAE16006 to N.M., Instituto de Salud Carlos III (CardioCell, TerCel to N.M.), the Deutsche Forschung Gemeinschaft (SFB 1027 to A.d.C.) and Obra Social ‘La Caixa’. IBEC is recipient of a Severo Ochoa Award of Excellence from the MINECO.

**Reviewer information** *Nature* thanks U. Schwarz, M. Théry and the other anonymous reviewer(s) for their contribution to the peer review of this work.

**Author contributions** E.L., L.C., M.A. and X.T. conceived the study and designed experiments. E.L. and L.C. performed the experiments with the help of L.V., E.G. and N.M. E.L., M.G.-G. and M.U. developed the 3D traction microscopy algorithm. E.L. and M.G.-G. developed computational analysis tools. E.L. and L.C. processed and analysed the experimental data with the help of M.G.-G. S.K. and M.A. developed the theory and implemented the vertex model. B.L. contributed expertise in the implementation of the micropatterned substrates. R.V.N. and A.d.C. developed the photoactivatable derivative of Cytochalasin D. E.L., M.A. and X.T. wrote the manuscript. All authors helped with the interpretation of the results and commented the manuscript. M.A. and X.T. supervised the study.

**Competing interests:** The authors declare no competing interests.

#### **Additional information**

**Extended data** is available for this paper at

**Supplementary information** is available for this paper at

**Reprints and permissions information** is available at [www.nature.com/reprints](http://www.nature.com/reprints).

**Correspondence and requests for materials** should be addressed to M.A. or X.T.

**Publisher’s note:** Springer Nature remains neutral with regard to jurisdictional claims in published maps and institutional affiliations.

**Fig. 1 | Generation of epithelial domes of controlled size and shape.** **a**, Scheme of the process of dome formation. **b**, Top view of an array of  $15 \times 15$  epithelial domes ( $n = 10$ ). Scale bar, 1 mm. **c-e**, Confocal  $x-y$ ,  $y-z$  and  $x-z$  sections of MDCK cells expressing LifeAct-GFP (MDCK-LifeAct) epithelial domes with a circular basal shape and varying spacing ( $n = 10$ ). Scale bar, 100  $\mu\text{m}$ .

**Fig. 2 | Measurement of luminal pressure and dome tension.** **a**, Scheme of dome mechanics. The lumen is under uniform pressure  $\Delta P$  (black arrows) and the free-standing monolayer is under surface tension  $\sigma$  (yellow arrows). **b**, Traction vectors of a dome of MDCK-LifeAct cells. Top, lateral view. Bottom, 3D traction maps overlaid on a top view of the dome. Yellow arrows represent in-plane components and the colour map represents the vertical component. Scale bar, 50  $\mu\text{m}$ . Scale arrows, 150 Pa (representative of  $n = 13$  domes). **c, d**, Traction vectors exerted by MDCK-LifeAct cells before (control) and after a 5-min incubation with 30  $\mu\text{M}$  of Y-27632. Scale bar, 50  $\mu\text{m}$ . Scale arrows, 75 Pa. **e-g**, Time evolution of dome volume and curvature (**e**), pressure (**f**) and tension (**g**) before (control) and after adding Y-27632. The time points corresponding to **c, d** are labelled in **e-g** (representative of  $n = 3$  domes).

**Fig. 3 | Constitutive relation between dome tension and strain.** **a**, Spontaneous time evolution of tractions in a MDCK-LifeAct dome ( $y-z$  section). Scale bar, 50  $\mu\text{m}$ . Scale arrows, 150 Pa. Regions in the dome monolayer that lack fluorescence signal correspond to unlabelled cells, not to gaps. **b-d**, Time evolution of spontaneous fluctuations in dome volume (**b**), pressure  $\Delta P$  (**c**) and surface tension  $\sigma$  (**d**) (representative of  $n = 9$  domes). **e**, Surface tension in the free-standing sheet as a function of nominal areal strain of the dome  $\varepsilon_d$  ( $n = 9$  domes, each sampled over various time points). The solid line and shaded area indicate mean  $\pm$  s.d. obtained by binning the data ( $n = 14$  points per bin). **f**, Normalized dome surface tension as a function of areal strain calculated with the vertex model. The dashed blue line represents the cellular constitutive relation in equation (1), based on a sheet of identical hexagonal cells under uniform strain ( $\varepsilon_d = \varepsilon_c$ ). The solid red line is the result of a multicellular computational vertex model for a dome with an initial geometry that was obtained experimentally. Insets show the computed dome shape at 50% (left) and 300% (right) nominal areal strain. **g**, Scheme of an idealized monolayer undergoing uniform equibiaxial stretching, representing model assumptions.

**Fig. 4 | Epithelial domes exhibit superelasticity.** **a**, Cell strain  $\varepsilon_c$  versus dome strain  $\varepsilon_d$  during a deflation event for a subset of cells. Coloured curves correspond to cells labelled in **b**. Dashed line,  $\varepsilon_c = \varepsilon_d$ . Inset shows variance (var) of  $\varepsilon_c$  versus  $\varepsilon_d$ . **b**, Deflating dome of MDCK–CAAX cells (see ‘Cell culture’ in Methods). Scale bar, 50  $\mu\text{m}$ . **c**, Model prediction of stretch-induced cortical dilution. **d**, Sum of intensity projection and confocal section of a dome stained with phalloidin for F-actin. Scale bar, 50  $\mu\text{m}$ . **e**, Zoom of representative cells. Scale bar, 10  $\mu\text{m}$ . **f**, F-actin intensity along the bands marked in **e**. AU, arbitrary units. **g**, Normalized density of cortical F-actin (stained with phalloidin) versus cellular strain ( $n = 68$  cells from 5 domes). **h**, Normalized density of cortical F-actin (SiR-actin) versus cellular strain during swelling (upward triangles) and de-swelling (downward triangles).  $n = 26$  cells from 7 domes. Solid line and shaded area in **g**, **h** indicate mean  $\pm$  s.d. **i**, Live imaging of the cortex (SiR-actin) at two instants during swelling. **j**, Intensity profiles along bands shown in **i**. **k**, Non-monotonic cellular constitutive relation predicted by the vertex model, accounting for softening by cortical depletion and re-stiffening at extreme cellular strains (blue line). Dome tension–strain relationship for the multicellular computational version of the same model (red line). Labels R1 to R4 correspond to panels shown in **q** and **r**. **l–n**, Dome of MDCK cells expressing keratin-18-GFP (green) stained for F-actin (phalloidin, red), and nuclei (Hoechst, blue) ( $n = 3$ ). Scale bar, 10  $\mu\text{m}$  (**l**, **n**), 50  $\mu\text{m}$  (**m**). **o**, **p**, Changes in cell area after laser cuts of keratin bundles for weakly stretched (blue,  $n = 8$ ) and superstretched cells (red,  $n = 7$ ), represented as cell area before and after cuts (**o**) and as normalized cell-area increment (**p**).  $**P = 0.0023$ ,  $***P < 0.0003$ , NS, not significant (**o**,  $P = 0.3282$ ). Two-tailed Mann–Whitney tests. Mean  $\pm$  s.d. **q**,  $\varepsilon_c$  versus  $\varepsilon_d$  from the vertex model. Inset, variance of  $\varepsilon_c$  versus  $\varepsilon_d$ . **r**, Bottom, computed geometries during deflation. Top, effective potential energy landscape of active origin. This landscape exhibits two wells at sufficiently high tension, corresponding to barely stretched and superstretched cellular states.

## METHODS

No statistical methods were used to predetermine sample size. The experiments were not randomized and investigators were not blinded to allocation during experiments and outcome assessment.

### **Fabrication of soft silicone gels**

Soft elastomeric silicone gels were prepared using a protocol based on previous publications<sup>29–32</sup>. In brief, a silicone elastomer was synthesized by mixing a 1:1 weight ratio of CY52-276A and CY52-276B polydimethylsiloxane (Dow Corning Toray). After degassing for 5 min, the gel was spin-coated on glass-bottom dishes (35-mm, no. 0 coverslip thickness, Mattek) for 90 s at 400 rpm. The samples were then cured at 80 °C for 1 h. The substrates were kept in a clean, dust-free and dry environment and they were always used within 4 weeks of fabrication.

### **Coating the soft PDMS substrate with fluorescent beads**

After curing, the soft PDMS was treated with (3-aminopropyl)triethoxysilane (APTES, Sigma-Aldrich, cat. no. A3648) diluted at 5% in absolute ethanol for 3 min, rinsed 3 times with ethanol 96%, and dried in the oven for 30 min at 60 °C. Samples were incubated for 5 min with a filtered (220 nm) and sonicated solution of 200-nm-diameter red fluorescent carboxylate-modified beads (FluoSpheres, Invitrogen) in sodium tetraborate (3.8 mg/ml, Sigma-Aldrich), boric acid (5 mg/ml, Sigma-Aldrich) and 1-ethyl-3-(3-dimethylaminopropyl)carbodiimide (EDC, 0.1 mg/ml, Sigma-Aldrich), as previously described<sup>29</sup>. Next, gels were rinsed 3 times with type-1 water and dried in the oven for 15 min at 60 °C. Beads were passivated by incubating the samples with tris-buffered saline (TBS, Sigma-Aldrich) 1% solution for 20 min at room temperature. Finally, substrates were rinsed again 3 times with type-1 water and dried in the oven for 15 min at 60 °C.

### **Soft PDMS stiffness measurements**

Gel stiffness was measured by indenting the gel with a large metal sphere (diameter, 1,000 μm) of known mass. The indentation caused by the weight of the sphere was determined using confocal microscopy. From the measured indentation and sphere mass, we obtained Young's modulus by applying Hertz theory, corrected for the finite thickness of the gel<sup>33</sup>. We found a Young's modulus of  $2.9 \pm 0.5$  kPa (mean  $\pm$  s.d.,  $n = 6$ ), in good agreement with published data<sup>29–32,34,35</sup>.

### **Cell patterning on soft PDMS**

PDMS patterning stamps were incubated with a fibronectin solution at 40 μg/ml (fibronectin from human plasma, Sigma-Aldrich) for 1 h. Next, the protein was transferred to poly vinyl alcohol (PVA, Sigma-Aldrich) membranes which were then placed in contact with the gel surface for 1 h. Membranes were dissolved and the surface was passivated at the same time using Pluronic F127 (Sigma-Aldrich) 0.2% w/v overnight at 4 °C. Afterwards, the soft silicone gels

were washed with phosphate-buffered saline (PBS, Sigma-Aldrich) and incubated with cell culture medium for 30 min. For cell seeding, the culture medium was removed and a 70- $\mu$ l drop containing  $\sim$ 150,000 cells was placed on the soft PDMS. Fifty minutes after seeding, the unattached cells were washed away using PBS and more medium was added. Cells were seeded at least 48 h before experiments.

### **PDMS patterning stamps**

PDMS (Sylgard, Dow Corning) stamps for micropatterning were fabricated. In brief, SU8-50 masters containing cylinders that were 80  $\mu$ m or 100  $\mu$ m in diameter were raised using conventional photolithography. Uncured PDMS was poured on the masters and cured for 2 h at 65 °C. PDMS was then peeled off from the master and kept at room temperature in a clean and dust-free environment until use.

### **Three-dimensional traction microscopy**

Three-dimensional traction forces were computed using traction microscopy with finite gel thickness<sup>36,37</sup>. To account for both geometrical and material nonlinearities, a finite element method (FEM) solution was implemented. Confocal stacks of the fluorescent beads covering the gel surface were taken with  $z$ -step = 0.3  $\mu$ m and total depth of 15  $\mu$ m. A 3D displacement field of the top layer of the gel between any experimental time point and its relative reference image (obtained after cell trypsinization) were computed using home-made particle imaging velocimetry software based on an iterative algorithm with a dynamic interrogation window size and implementing convergence criteria based on image intensity as described in previous publications<sup>38</sup>. Results for the normal traction inside the dome were compared to analytical solutions for a liquid droplet over an elastic substrate with finite thickness<sup>39-42</sup>.

### **Cell culture**

MDCK strain II and Caco-2 cells were used. To visualize specific cell structures, the following stable fluorescent cell lines were used: MDCK expressing LifeAct-GFP (MDCK-LifeAct) to visualize the actin cytoskeleton, MDCK expressing CIBN-GFP-CAAX to visualize the plasma membrane (MDCK-CAAX), MDCK expressing keratin-18-GFP (MDCK-K18) to visualize intermediate filaments. All MDCK lines were cultured in minimum essential medium with Earle's Salts and L-glutamine (Gibco) supplemented with 10% v/v fetal bovine serum (FBS; Gibco), 100  $\mu$ g/ml penicillin and 100  $\mu$ g/ml streptomycin. Selection antibiotic geneticin (Thermo

Fisher Scientific) was added at 0.5 mg/ml to LifeAct stable cell lines. Cells were maintained at 37 °C in a humidified atmosphere with 5% CO<sub>2</sub>. Live imaging of F-actin was performed by incubating cells (12 h, 100 nM) using live cell fluorogenic F-actin labelling probe (SiR-actin, Spirochrome). Caco-2 cells were imaged using Bodipy FL C16 dye (1 μM, 1h incubation, Thermo Fisher Scientific). MDCK–LifeAct cells were obtained from the laboratory of B. Ladoux. MDCK keratin-18–GFP cells were obtained from the laboratory of G. Charras. MDCK–CAAX cells were obtained by viral infection of CIBN–GFP–CAAX. Caco-2 cells were bought at Sigma Aldrich (86010202). Cell lines tested negative for mycoplasma contamination. All MDCK cell lines were authenticated by the laboratories that provided them. Caco-2 cells were authenticated by the provider (Sigma Aldrich, from the ECACC).

### **Pharmacological interventions and osmotic shocks**

To perturb actomyosin contractility cells were treated with Rho kinase inhibitor Y-27632 (InSolution Calbiochem, Merck-Millipore, 30 μM, 5-min incubation). To inhibit ARP2/3 complex, cells were treated with CK666 (Sigma Aldrich, 100 μM, 1-h incubation). To perturb the osmolarity, D-mannitol (Sigma-Aldrich, final concentration 100 mM) was added to the medium. To weaken cell–cell junctions, EGTA (Sigma-Aldrich, final concentration 2 mM, 30-min incubation) was added to the medium.

### **Cell immunofluorescence**

MDCK cells were fixed with 4% paraformaldehyde in PBS for 10 min at room temperature and permeabilized using 0.1% Triton X100 (Sigma-Aldrich) in PBS for 10 min at room temperature. Cells were blocked in 1% bovine serum albumin (BSA, Sigma-Aldrich) in PBS for 1 h (at room temperature). Phalloidin (Alexa Fluor 555 phalloidin, ThermoFisher Scientific) was then added at 1:1,000 dilution in PBS and incubated for 30 min at room temperature. To identify nuclei, cells were then incubated for 10 min in a Hoechst solution (Hoechst 33342, ThermoFisher Scientific) at 1:2,500 dilution in PBS. Images were acquired with a spinning disk confocal microscope using a Nikon 60× oil 1.4 numerical aperture (NA) lens.

### **Time-lapse microscopy**

Multidimensional acquisition for traction force measurements was performed using an inverted Nikon microscope with a spinning disk confocal unit (CSU-W1, Yokogawa), Zyla sCMOS camera (Andor, image size 2,048 × 2,048 pixels) using a Nikon 40 × 0.75 NA air lens. The

microscope was equipped with temperature control and CO<sub>2</sub> control, using Andor iQ3 or Micro-Manager software<sup>43</sup>.

### **Laser ablation**

The set-up used has previously been described<sup>44</sup>. In brief, MDCK keratin-18–GFP cells were cultured on thin PDMS micropatterned substrates and allowed to form domes. We then used a sub-nanosecond ultraviolet pulsed laser to ablate individual filament bundles in weakly stretched and superstretched cells. Immediately after ablation we monitored the time evolution of keratin filaments, and we obtained bright-field images of the domes to measure cell area. Experiments were performed at 37 °C and 5% CO<sub>2</sub>.

### **Photoactivatable cytochalasin D**

We used a phototriggerable derivative of cytochalasin D that includes a nitroveratryloxycarbonyl photoremovable group located at the hydroxyl group at C7 of cytochalasin D. Attachment of the chromophore renders cytochalasin D temporarily inactive. Upon light exposure, cytochalasin D becomes active and causes local depolymerization of the actin cytoskeleton. For experiments, MDCK–CAAX domes were incubated with SiR–actin to visualize the cortical cytoskeleton. Individual cells were illuminated with a 405-nm laser to activate cytochalasin D. After the pulse, the cell area and actin cytoskeleton were visualized using time-lapse microscopy (63 × oil, Zeiss LM 880).

### **Image analysis**

Fiji software was used to perform the image analysis<sup>45</sup>. The pairwise stitching plugin was used to create 3D montages, the maximum intensity *z*-projection and the sum-slices *z*-projection were used where appropriate. Actual cell areas were computed from *z*-projections using the methodology described in Supplementary Note 4.

### **Animals**

Animal care and experiments were carried out according to protocols approved by the Ethics Committee on Animal Research of the Science Park of Barcelona (PCB), Spain (Protocol number 7436). Outbred B6CBAF1/JRj mice (male and females of 5–6 weeks of age) were obtained from Janvier Labs. Mice were kept in a 12 h light:dark cycle (lights on 7:00–19:00) with ad libitum access to food and water.



### **Embryo collection and in vitro culture**

For embryo collection, superovulation was induced in B6CBAF1/JRj female mice by intraperitoneal injection of 7.5 I.U. of pregnant mare serum gonadotropin (PMSG), followed—after 48h—by 7.5 I.U. of human chorionic gonadotropin (hCG). Superovulated females were then paired with male mice, and subsequently euthanized by cervical dislocation 20 h after hCG injection. Then, one-cell stage embryos (zygotes) were collected from the excised oviducts into medium containing 0.1% (w/v) hyaluronidase (Sigma) to remove cumulus cells under a dissection microscope. Recovered zygotes were cultured in micro-droplets of culture medium covered with mineral oil at 37 °C and 5% CO<sub>2</sub> until the blastocyst stage. No randomization nor blinding were performed as experiments did not involve comparisons between groups. Experiments were reproduced four times.

### **Blastocyst immunofluorescence**

Blastocysts at different degrees of development were fixed with 4% paraformaldehyde (PFA) (Aname) for 20 min at room temperature. Then, fixed blastocysts were washed three times with PBS containing 1% bovine serum albumin (Sigma), 2% goat serum (Sigma) and 0.01% Triton X-100 (Sigma), referred to as blocking buffer. Next, blastocysts were permeabilized with 2.5% Triton X-100 (Sigma) in PBS for 30 min at room temperature and subsequently washed three times with blocking buffer. Blastocysts were incubated overnight at 4 °C in anti-E-cadherin primary antibody (610181, BD Biosciences), diluted 1:50 in blocking buffer. The following day, blastocysts were washed three times with blocking buffer and incubated for 90 min at 37 °C in Alexa Fluor (A) 488-conjugated secondary antibody (A21202, Thermo Fisher), diluted 1:200 in blocking buffer. Nuclei were counterstained with DAPI (D1306, Life Technologies) for 30 min. Image acquisition was performed in a SP5 Leica microscope or a Zeiss LSM780 confocal microscope using a plan-apochromat 40× oil DIC M27 objective.

### **Code availability**

Matlab analysis procedures are available from the corresponding authors on reasonable request.

### **Reporting summary**

Further information on research design is available in the Nature Research Reporting Summary linked to this paper.

### Data availability

The data that support the findings of this study are available from the corresponding authors on reasonable request.

29. Style, R. W. et al. Traction force microscopy in physics and biology. *Soft Matter* **10**, 4047–4055 (2014).
30. Style, R. W., Hyland, C., Boltyanskiy, R., Wettlaufer, J. S. & Dufresne, E. R. Surface tension and contact with soft elastic solids. *Nat. Commun.* **4**, 2728 (2013).
31. Mertz, A. F. et al. Cadherin-based intercellular adhesions organize epithelial cell-matrix traction forces. *Proc. Natl Acad. Sci. USA* **110**, 842–847 (2013).
32. Vedula, S. R. et al. Epithelial bridges maintain tissue integrity during collective cell migration. *Nat. Mater.* **13**, 87–96 (2014).
33. Long, R., Hall, M. S., Wu, M. & Hui, C. Y. Effects of gel thickness on microscopic indentation measurements of gel modulus. *Biophys. J.* **101**, 643–650 (2011).
34. Mertz, A. F. et al. Scaling of traction forces with the size of cohesive cell colonies. *Phys. Rev. Lett.* **108**, 198101 (2012).
35. Bergert, M. et al. Confocal reference free traction force microscopy. *Nat. Commun.* **7**, 12814 (2016).
36. del Álamo, J. C. et al. Three-dimensional quantification of cellular traction forces and mechanosensing of thin substrata by Fourier traction force microscopy. *PLoS ONE* **8**, e69850 (2013).
37. Álvarez-González, B. et al. Three-dimensional balance of cortical tension and axial contractility enables fast amoeboid migration. *Biophys. J.* **108**, 821–832 (2015).
38. Bar-Kochba, E., Toyjanova, J., Andrews, E., Kim, K.-S. & Franck, C. A fast iterative digital volume correlation algorithm for large deformations. *Exp. Mech.* **55**, 261–274 (2015).
39. Yu, Y. S. & Zhao, Y. P. Elastic deformation of soft membrane with finite thickness induced by a sessile liquid droplet. *J. Colloid Interface Sci.* **339**, 489–494 (2009).
40. Das, S., Marchand, A., Andreotti, B. & Snoeijer, J. H. Elastic deformation due to tangential capillary forces. *Phys. Fluids* **23**, 072006 (2011).

41. Lubarda, V. A. Mechanics of a liquid drop deposited on a solid substrate. *Soft Matter* **8**, 10288–10297 (2012).
42. Yu, Y.-s. Substrate elastic deformation due to vertical component of liquid-vapor interfacial tension. *Appl. Math. Mech.* **33**, 1095–1114 (2012).
43. Edelstein, A. D. et al. Advanced methods of microscope control using  $\mu$ Manager software. *J. Biol. Methods* **1**, e10 (2014).
44. Colombelli, J., Grill, S. W. & Stelzer, E. H. K. Ultraviolet diffraction limited nanosurgery of live biological tissues. *Rev. Sci. Instrum.* **75**, 472–478 (2004).
45. Schindelin, J. et al. Fiji: an open-source platform for biological-image analysis. *Nat. Methods* **9**, 676–682 (2012).

**Extended Data Fig. 1 | The number of cells in the domes does not change significantly in time.** **a-c**, Confocal  $x$ - $y$ ,  $y$ - $z$  and  $x$ - $z$  sections of domes of MDCK–CAAX cells, with rectangular basal shapes and varying size. Scale bar, 100  $\mu\text{m}$  (representative of  $n = 3$  micropatterned substrates). **d**, Time evolution (0, 60 and 120 min) of a representative dome with a star-shaped footprint. The patterned footprint (yellow) was obtained from images of the fibrinogen-labelled substrate. Each row shows a different  $z$ -plane (labelled by dotted yellow lines in the  $x$ - $y$  profiles in **e** ( $n = 3$  micropatterned substrates)). Scale bar, 50  $\mu\text{m}$ . **e**, Time evolution (0, 60 and 120 min) of the same star-shaped dome, showing the rare delamination of a single cell (red rectangle) at one tip of the star. Images are maximum intensity projections with confocal  $x$ - $z$  and  $y$ - $z$  sections along the yellow dashed lines ( $n = 3$  micropatterned substrates). Scale bar, 50  $\mu\text{m}$ . **f**, Quantification of the number of cells in circular domes at two time points 12 h apart ( $n = 4$  domes). NS, not significant ( $P = 0.4571$ ), two-tailed Mann–Whitney test. Data are shown as mean  $\pm$  s.d.

**Extended Data Fig. 2 | Dome response to inhibition of tension and weakening of cell–cell adhesion.** **a**, Time evolution of surface tension and volume of a representative dome in response to Y27632 (30  $\mu\text{M}$ , added at  $t = 0$  min). **b**, Cellular areal strain  $\varepsilon_c$  as a function of dome nominal areal strain  $\varepsilon_d$  during dome swelling. Only a subset of cells is represented and most cells with

$\varepsilon_c < \varepsilon_d$  have been omitted for clarity. Coloured lines represent the cells labelled in **c**. Dashed line represents the relation  $\varepsilon_c = \varepsilon_d$ . The inset represents the variance of  $\varepsilon_c$  within the dome as a function of  $\varepsilon_d$ . **c**, Maximum intensity projection and  $x$ - $z$  and  $y$ - $z$  confocal sections of an epithelial dome of MDCK-CAAX cells before (-1 min) and after (12 min and 26 min) addition of Y27632 (30  $\mu$ M, added at  $t = 0$  min). The time evolution of coloured cells is depicted in **b** using the same colour code. Scale bars, 50  $\mu$ m. Data are representative of  $n = 3$  experiments. **d**, Maximum intensity projection and corresponding  $x$ - $z$  and  $y$ - $z$  profiles, showing the collapse of a dome of MDCK-CAAX cells after treatment with 2 mM EGTA (30 min and 35 min after the addition of EGTA). Data are representative of  $n = 3$  experiments. Scale bar, 50  $\mu$ m. **e**, After dome collapse, gaps (red arrowheads) were apparent at tricellular junctions. Scale bar, 10  $\mu$ m.

**Extended Data Fig. 3 | Dome volume dynamics during spontaneous fluctuations. a, c**, Time evolution of the dome volume in experiments that last 12 h (**a**) and 6 h (**c**). Cells are MDCK-LifeAct. **b, d**, Confocal  $x$ - $z$  sections of domes during these experiments. Data representative of  $n = 10$  experiments. Scale bars, 50  $\mu$ m.

**Extended Data Fig. 4 | Tension-strain relations in MDCK-CAAX and Caco2 cells. a**, Relation between surface tension and areal strain for MDCK-CAAX cells. Data include measurements at different time points from  $n = 9$  domes. The tension-strain relation is qualitatively similar to the one obtained for MDCK-LifeAct cells (Fig. 3e), with small quantitative differences. The solid line and shaded area indicate the mean  $\pm$  s.d. obtained by binning the data ( $n = 14$  points per bin). **b**, Image of a representative Caco2-cell dome labelled with Bodipy FL C16 dye ( $n = 3$  micropatterned substrates). Confocal  $x$ - $y$ ,  $x$ - $z$  and  $y$ - $z$  sections are shown. Scale bar, 50  $\mu$ m. **c**, Relation between surface tension and areal strain for Caco2 cells. Data include measurements at different time points from  $n = 6$  domes. Caco2 cells show a tensional plateau throughout the probed strain range. The solid line and shaded area indicate the mean  $\pm$  s.d. obtained by binning the data ( $n = 10$  points per bin).

**Extended Data Fig. 5 | Dome cells exhibit large strain heterogeneity. a**, Cellular areal strain  $\varepsilon_c$  as a function of dome nominal areal strain  $\varepsilon_d$  during dome swelling. Only a subset of cells is represented and most cells with  $\varepsilon_c < \varepsilon_d$  have been omitted for clarity. Coloured lines represent the cells labelled in **b**. Dashed line represents the relation  $\varepsilon_c = \varepsilon_d$ . The inset represents the variance of  $\varepsilon_c$  within the dome as a function of  $\varepsilon_d$ . **b**, Maximum intensity projection of an epithelial dome of

MDCK–CAAX cells at four different time points of the swelling event described in **a**. The time evolution of coloured cells is depicted in **a** using the same colour code. Scale bars, 50  $\mu\text{m}$ . **c**, **d**, represent the same as **a**, **b**, for a different dome of MDCK–CAAX cells during slow deflation. **e**, Coefficient of variation (CV) (defined as standard deviation divided by mean) of MDCK–CAAX cells in a 2D adherent cell monolayer, in weakly inflated domes (20–100% areal strain), and in highly inflated domes (100–150%). The coefficient of variation is a non-dimensional indicator of heterogeneity. The coefficient of variation was calculated by measuring area of 10 cells in  $n = 7$  cell monolayers,  $n = 7$  weakly inflated domes and  $n = 7$  highly inflated domes.  $**P = 0.0041$  (left),  $**P = 0.0041$  (right), two-tailed Mann–Whitney test. Data are shown as mean  $\pm$  s.d. **f**, **g**, Mouse blastocysts (labelled with E-cadherin) exhibiting heterogeneity in cell area in the trophectoderm, particularly during hatching (**g**) ( $n = 4$ ). Scale bars, 25  $\mu\text{m}$ .

**Extended Data Fig. 6 | Superstretched cells display a lower density of F-actin at the cortical surface.** **a–f**, Sum of intensity projection of epithelial domes stained with phalloidin for F-actin.  $n = 5$ . Scale bars, 50  $\mu\text{m}$ .

**Extended Data Fig. 7 | Inhibition of ARP2/3 does not affect area heterogeneity in domes of MDCK cells.** **a**, Coefficient of variation of the cell area in domes of MDCK–CAAX cells, treated with CK666 (100  $\mu\text{M}$  for 60 min), compared to control domes. The coefficient of variation is a non-dimensional indicator of heterogeneity. The coefficient of variation was calculated by measuring area of 10 cells in  $n = 6$  domes treated with CK666 and in  $n = 14$  control domes. NS, not significant ( $P = 0.1256$ ). Two-tailed Mann–Whitney test. Data are shown as mean  $\pm$  s.d. **b**, Dome nominal areal strain in domes of MDCK–CAAX cells, treated with CK666 (100  $\mu\text{M}$  for 60 min,  $n = 6$ ), compared to control domes ( $n = 14$ ). NS, not significant ( $P = 0.7043$ ). Two-tailed Mann–Whitney test. Data are shown as mean  $\pm$  s.d. **c**, Maximum intensity projections and  $x$ – $z$  sections of a representative control dome (left) and the same dome treated with CK666 100  $\mu\text{M}$  (60 min). Scale bar, 25  $\mu\text{m}$ .

**Extended Data Fig. 8 | Local perturbation of the actin cortex using photoactivatable cytochalasin D increases cell area.** **a** Time evolution of the normalized cell area in response to local photoactivation of cytochalasin D (black line, activation at  $t = 0$  min,  $n = 5$  domes; see Methods). The blue line shows the time evolution of control cells (same illumination protocol but no photoactivatable cytochalasin D in the medium,  $n = 8$  domes). The area was normalized to

the first time point. Solid lines and shaded areas indicate mean  $\pm$  s.d. At  $t = 21$  min, normalized cell areas were significantly different ( $*P = 0.0159$ , two-tailed Mann–Whitney test). **b**, Normalized cell area 21 min after photoactivation in three experimental conditions: photoactivated cells (black circles,  $n = 19$  cells from 5 domes), cells subjected to the same illumination protocol but without photoactivatable cytochalasin D in the medium (blue squares,  $n = 19$  cells from 8 domes) and cells with photoactivatable cytochalasin D in the medium but without illumination (red triangles,  $n = 24$  cells from 9 domes). Data include the immediate neighbours of the targeted cells because cytochalasin D quickly diffused after activation. \*\*\*\* $P < 0.0001$ , NS, not significant ( $P = 0.4130$ ), two-tailed Mann–Whitney test. Data are shown as mean  $\pm$  s.d. **c**, Representative photoactivation experiments showing the apex of one dome before ( $-12$  min) and after (6 min and 21 min) photoactivation of the cell marked with a yellow dashed rectangle ( $n = 5$ ). Top panels show the fluorescently labelled membrane and bottom panels show the SiR–actin channel. Note the increase in cell area and granulation in the SiR–actin channel (white arrowheads), which indicates disruption of the actin cortex. Scale bar, 15  $\mu\text{m}$ . **d**, Control experiment in which one cell at the apex of the dome (yellow dashed line) was subjected to the illumination protocol of **c** without photoactivatable cytochalasin D in the medium ( $n = 8$ ). Top panels show the fluorescently labelled membrane and bottom panels show the SiR–actin channel. Scale bar, 15  $\mu\text{m}$ . See also Supplementary Video 9.

**Extended Data Fig. 9 | Intermediate filaments reorganize in superstretched cells. a–f**, Immunofluorescence micrographs (see Methods)—represented using maximum intensity projection—of domes of MDCK keratin-18–GFP (in green) cells stained for F-actin (phalloidin, red), and nuclei (Hoechst, blue),  $n = 3$ . Scale bars, 50  $\mu\text{m}$ . **a, d**, Zoomed-in area (marked with a dashed white square in **b**) showing that the keratin-18 filament network links neighbouring cells and localizes at cell boundaries (white arrowheads). Scale bars, 10  $\mu\text{m}$ . **c, f**, Zoomed-in area (marked with a dashed white square in **e**) showing that keratin-18 filaments are taut (white arrowheads) and have reorganized, with nodes at the cell centre connecting different cells. Scale bars, 10  $\mu\text{m}$ .

**Extended Data Fig. 10 | Intermediate filaments stabilize cell shape in superstretched cells. a**, Representative MDCK keratin-18–GFP superstretched cell at the apex of a dome before (0 s) and after (90 s) laser cutting the keratin filament bundle marked in **b** with a white arrowhead. The yellow line marks the outline of the cell measured with bright-field imaging. Scale bar,

10  $\mu\text{m}$ . **b**, Magnified view of the region labelled in **a** with a dotted magenta rectangle. Scale bar, 5  $\mu\text{m}$ . **c**, Representative MDCK keratin-18–GFP weakly stretched cell at the apex of a dome before (0 s) and after (90 s) laser cutting the keratin filament bundle shown in **d**. The yellow line marks the outline of the cell measured with bright-field imaging. Scale bar, 10  $\mu\text{m}$ . **d**, Magnified view of the region labelled in **c** with a dotted magenta rectangle. The same laser cutting protocol and laser power were used to cut filaments in superstretched and weakly stretched cells.  $n = 5$ . Scale bar, 5  $\mu\text{m}$ . See Fig. 4o, p for quantification and statistics.

Figure 1

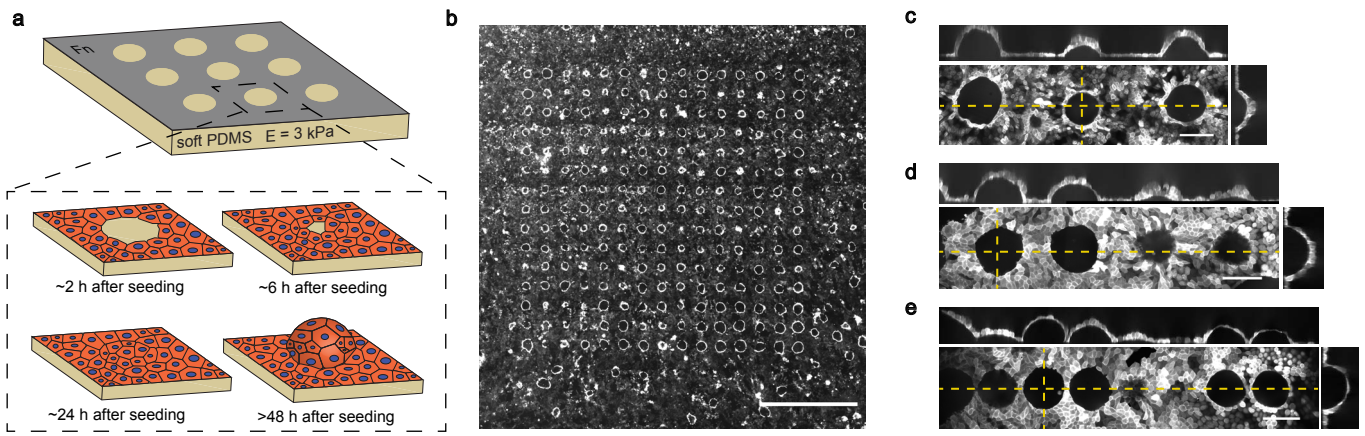
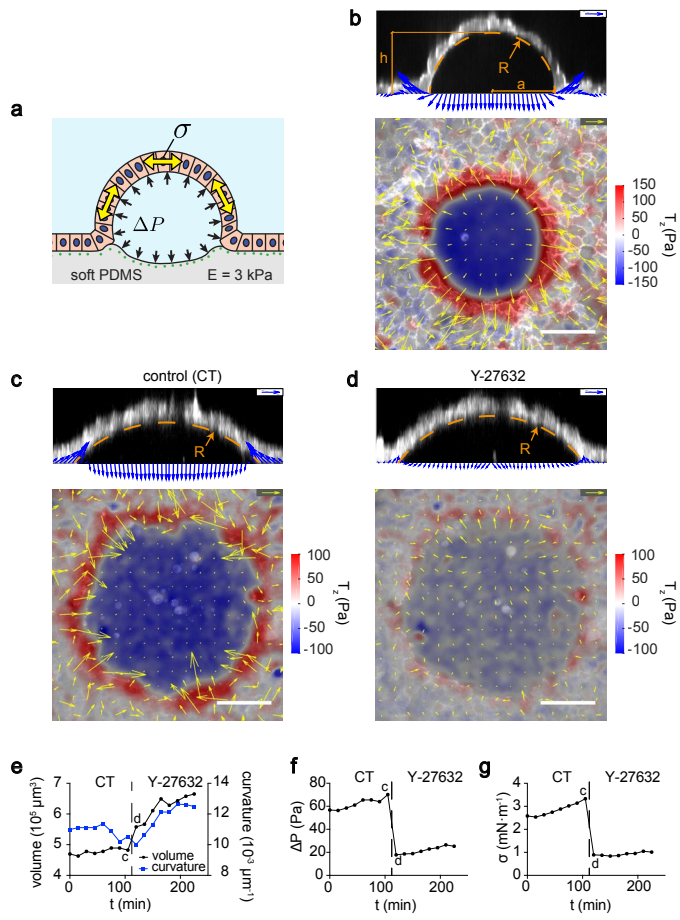
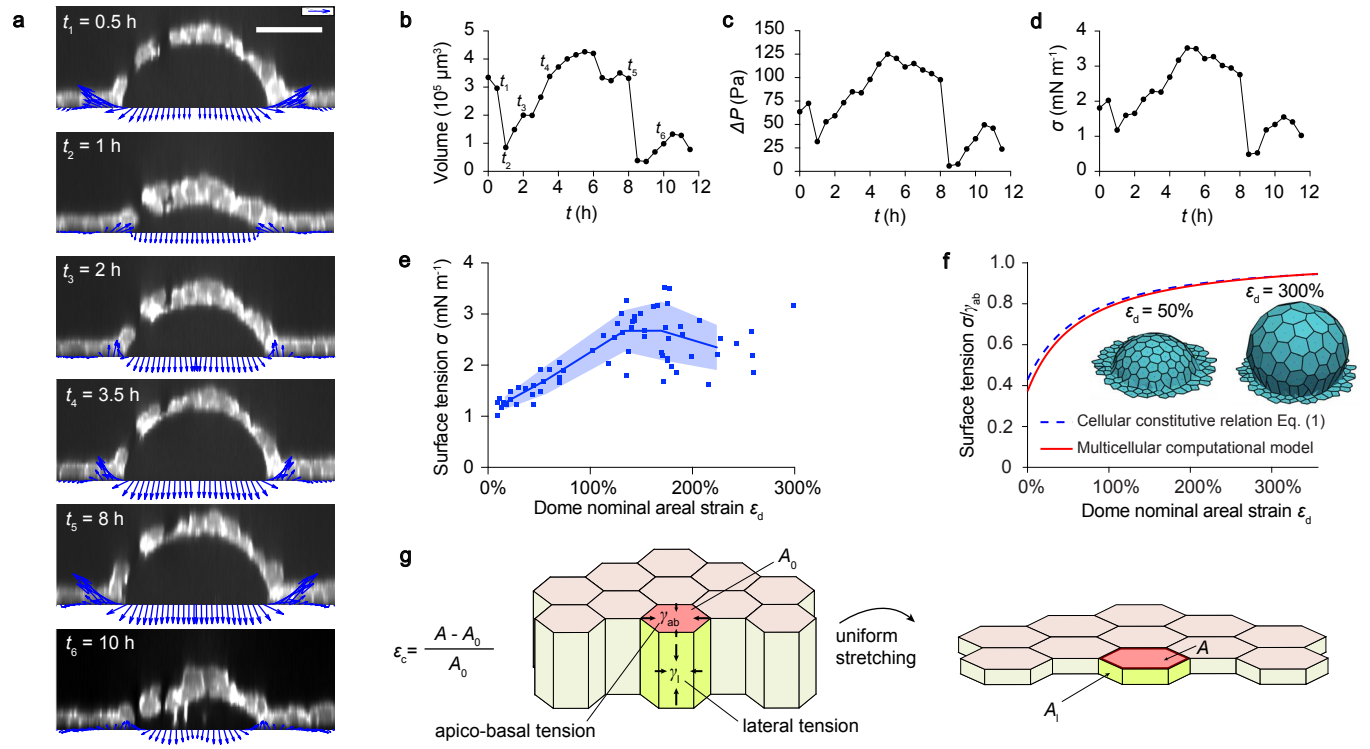




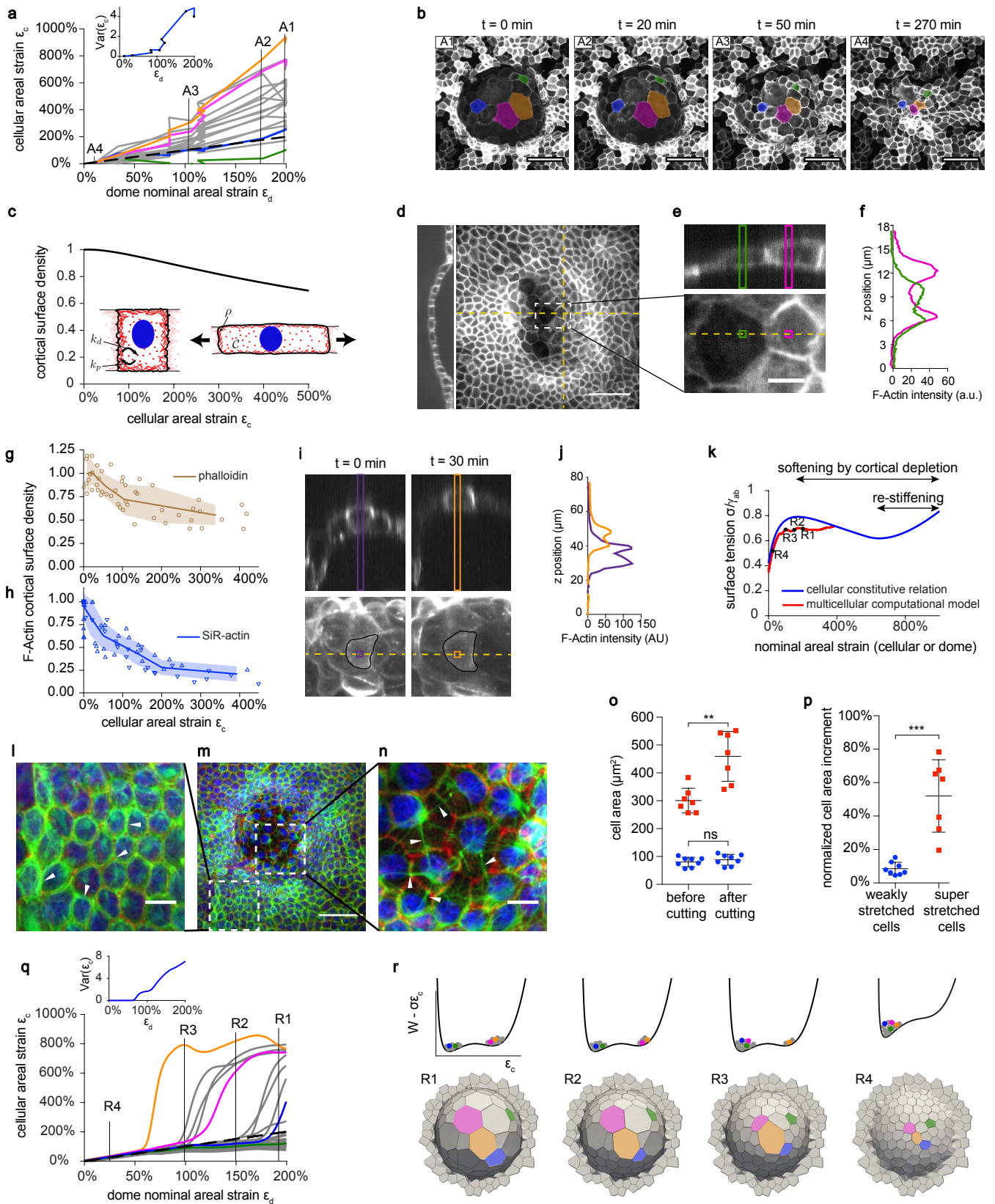
Figure 2



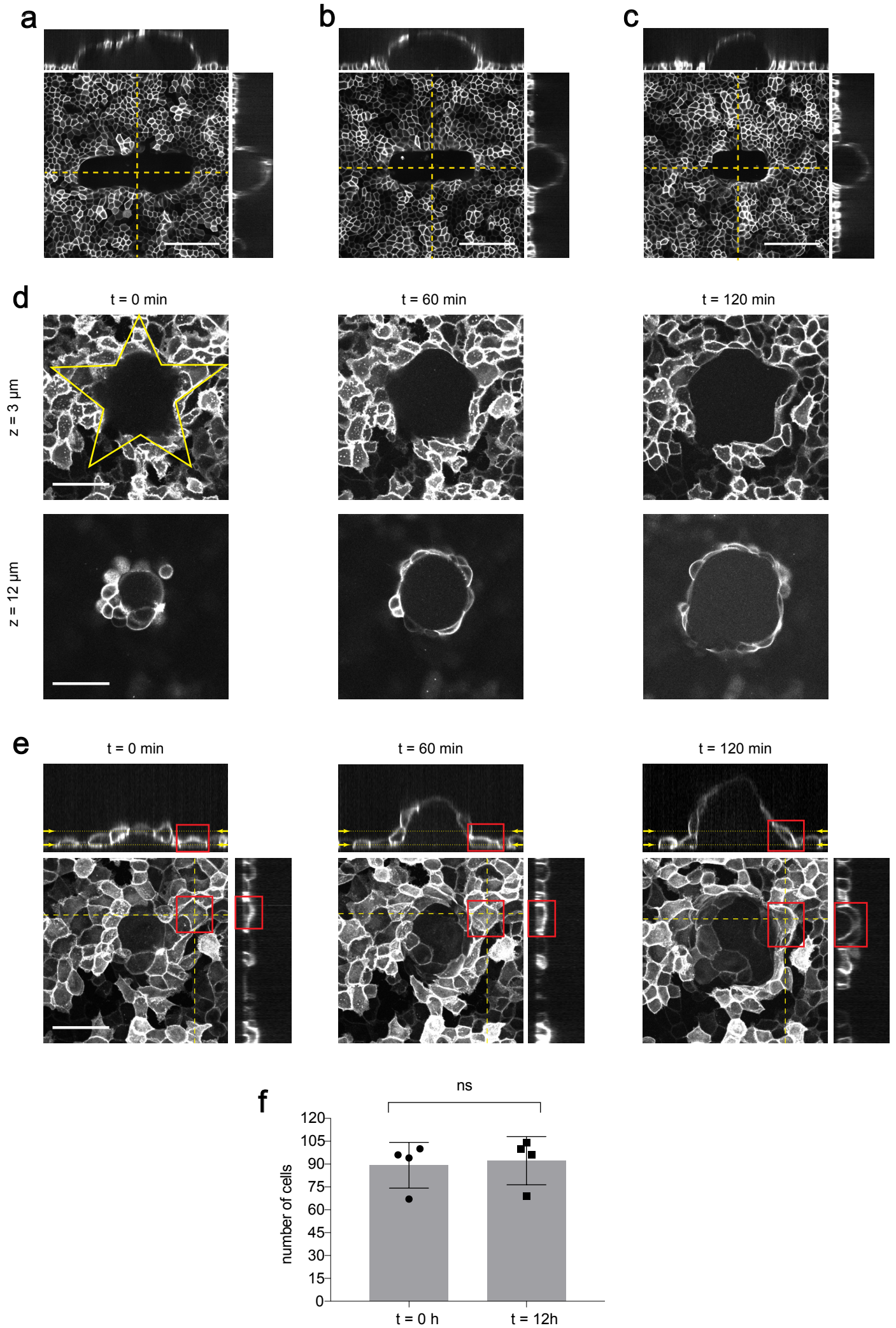
# Figure 3



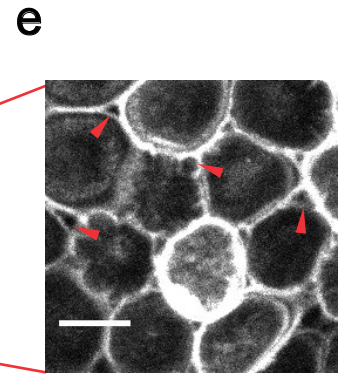
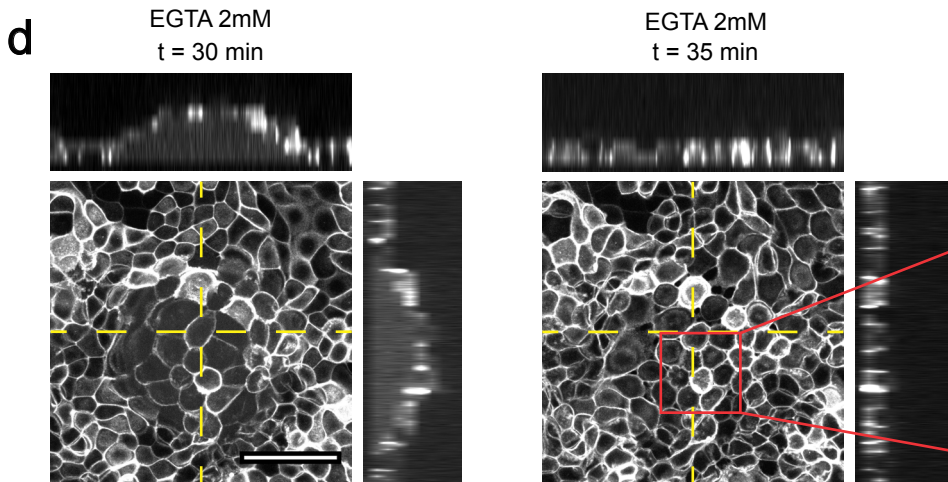
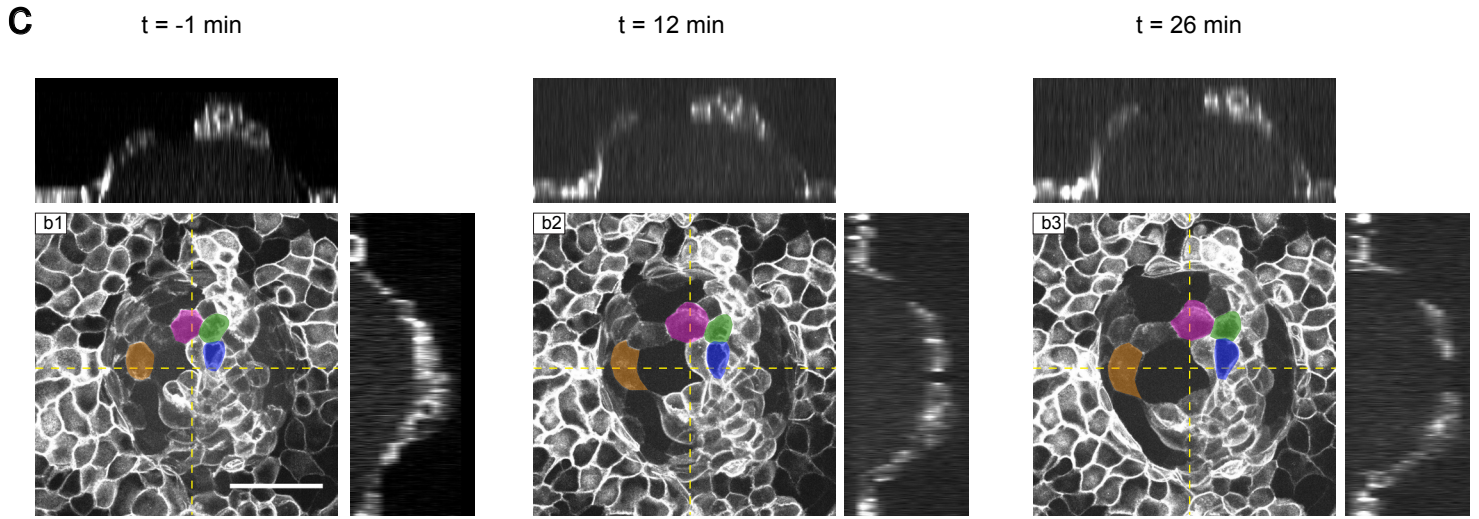
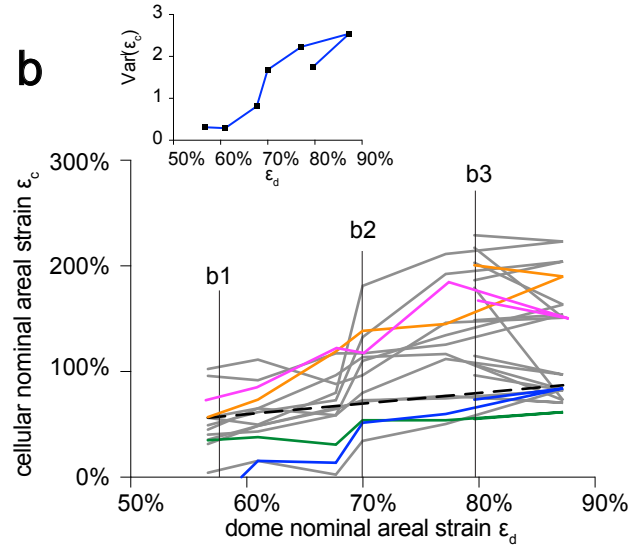
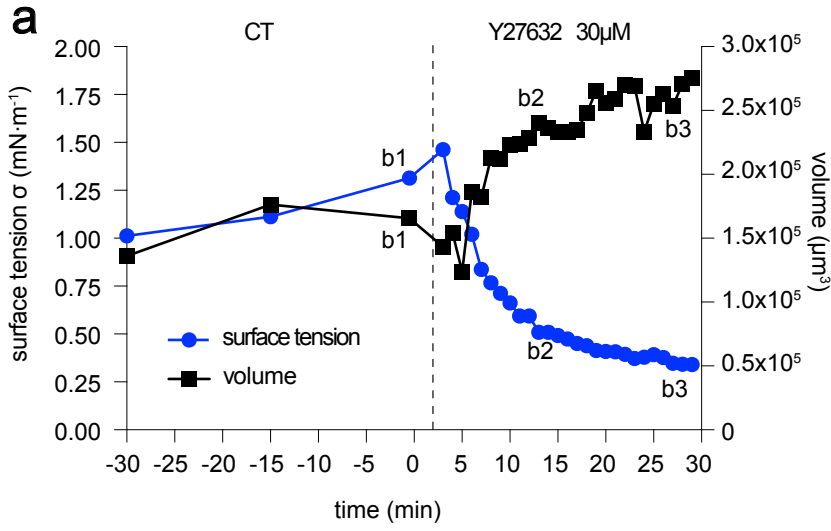
# Figure 4



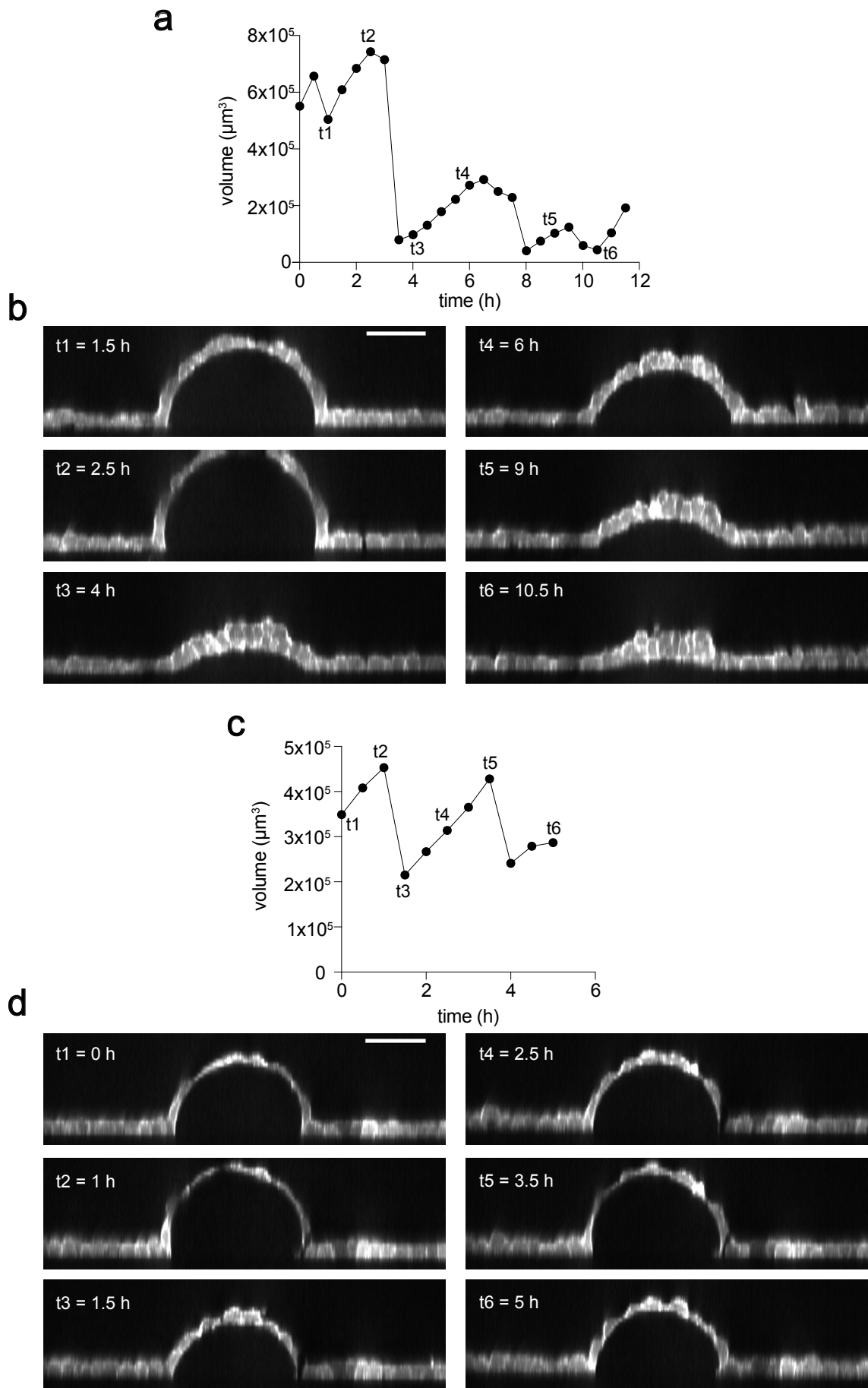
# Extended Data figure 1



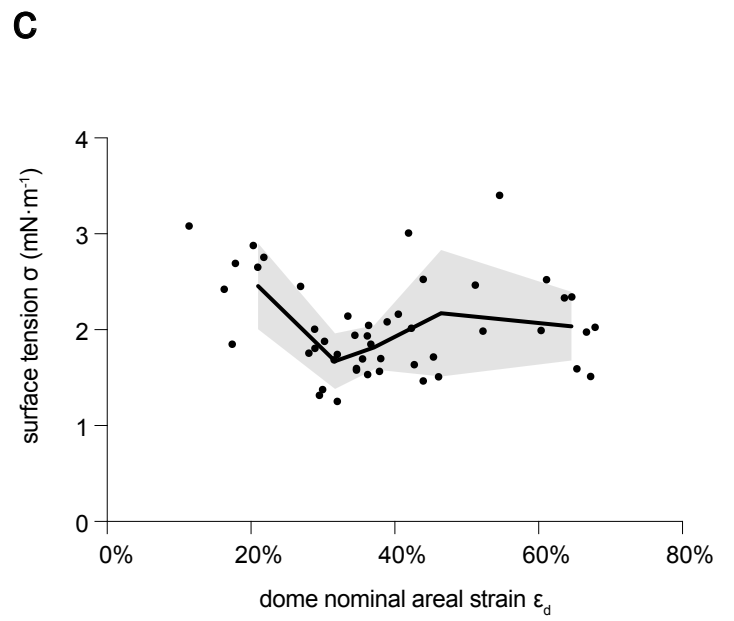
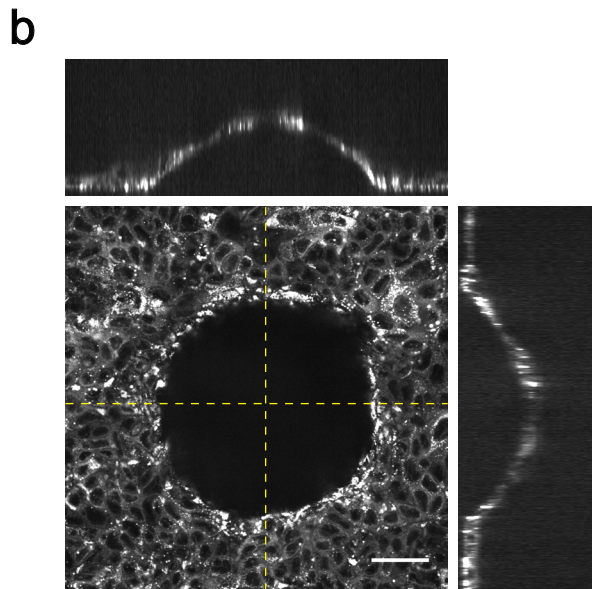
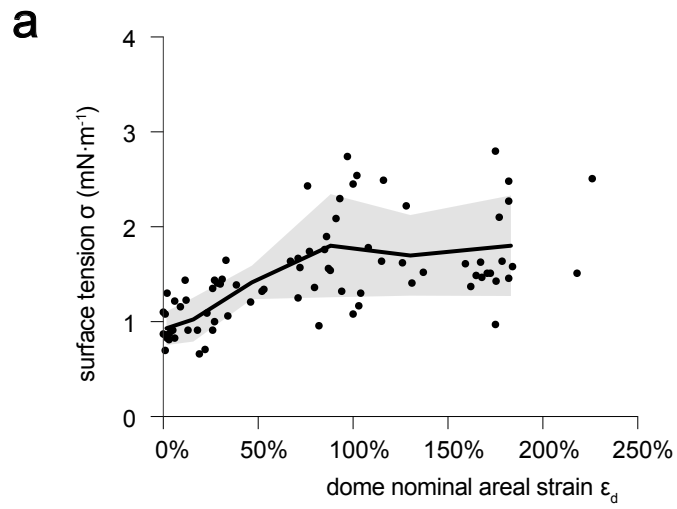
# Extended Data figure 2



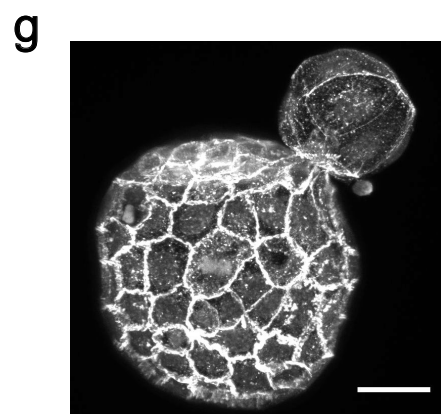
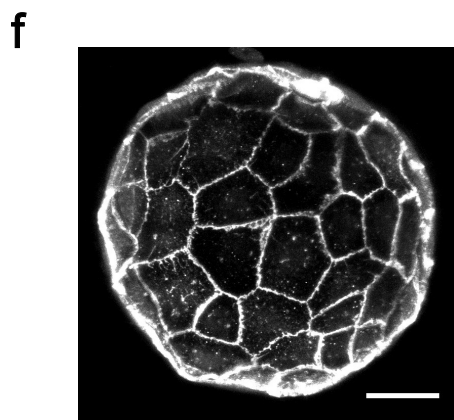
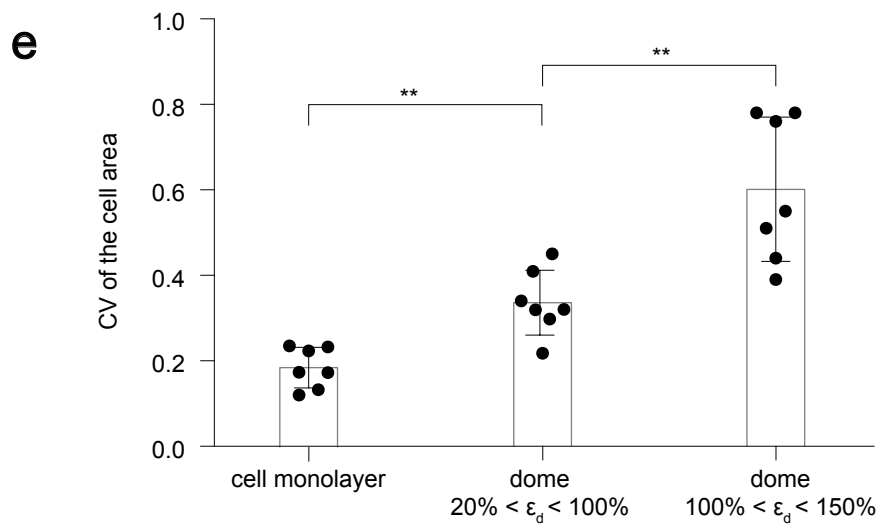
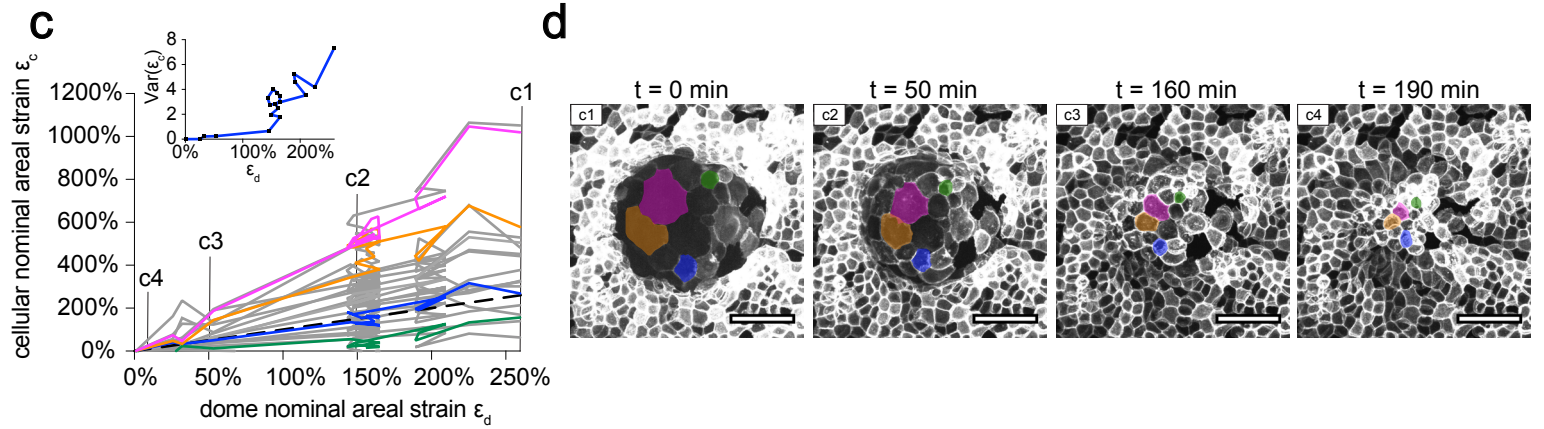
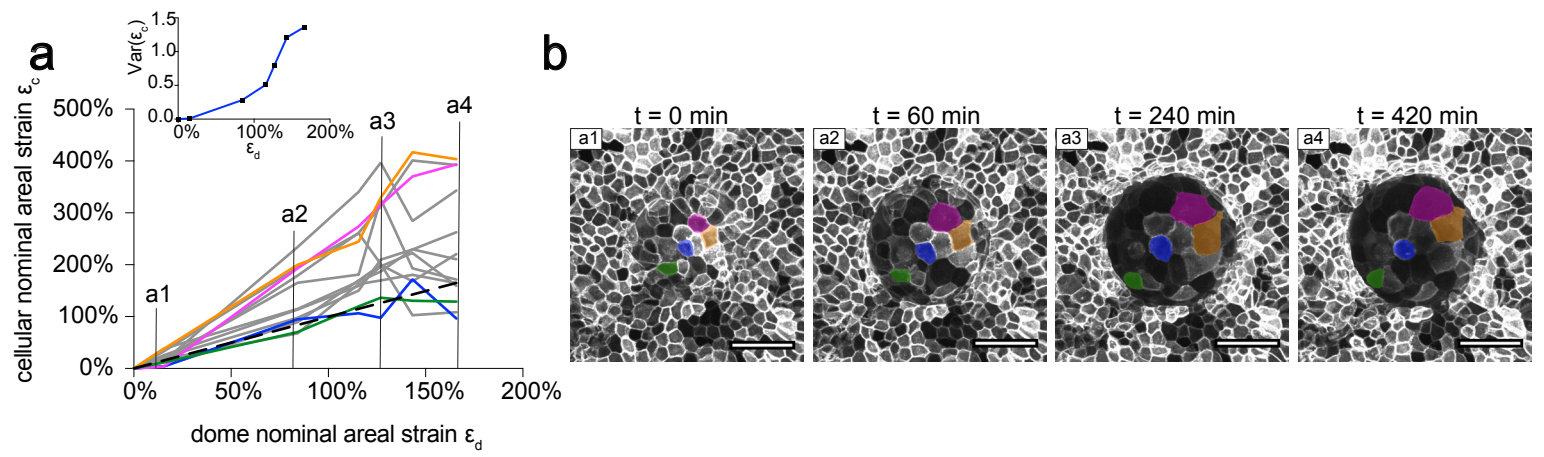
# Extended Data figure 3



# Extended Data figure 4



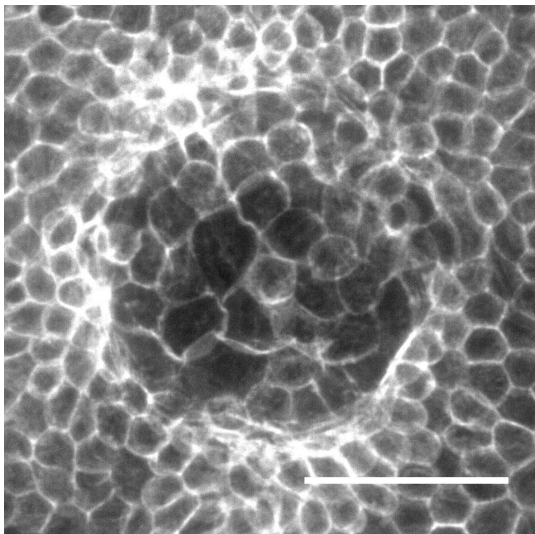
# Extended Data figure 5



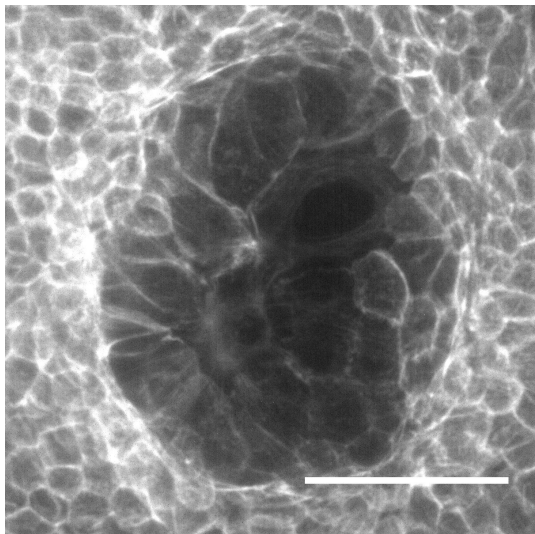


Extended Data figure 6

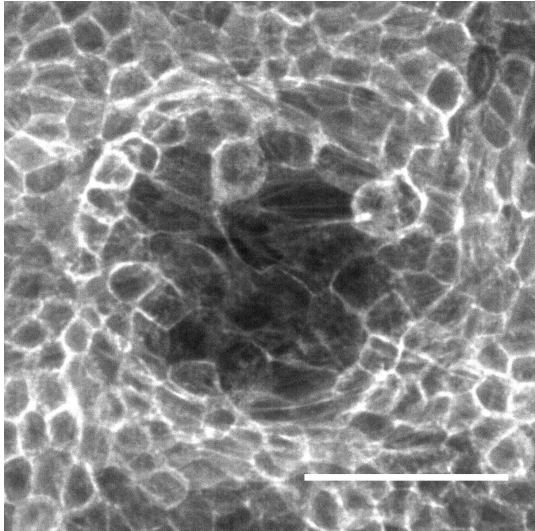
**a**



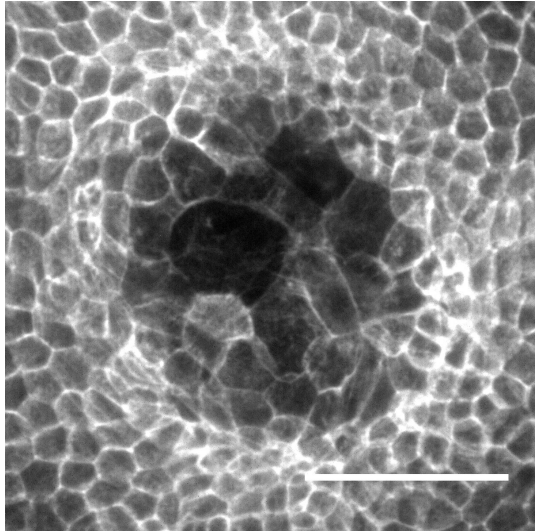
**b**



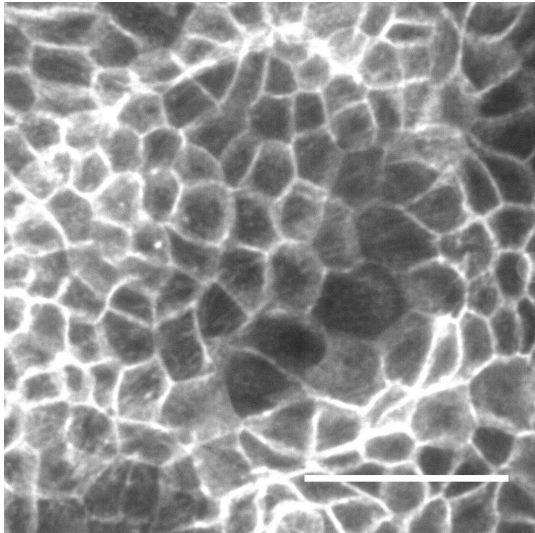
**c**



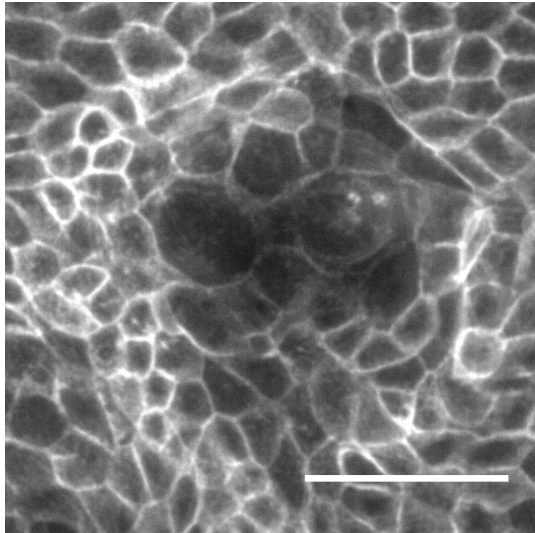
**d**



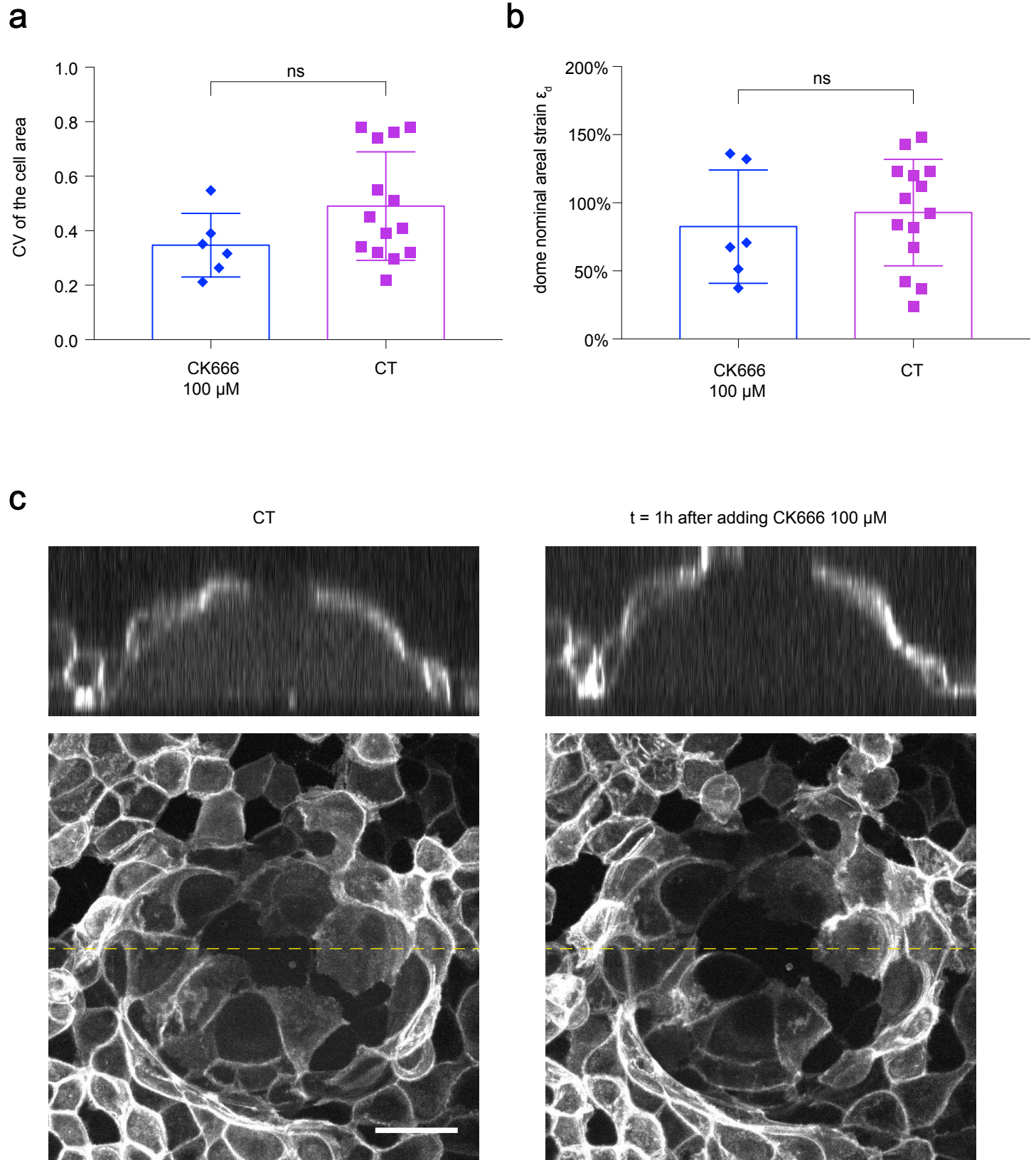
**e**



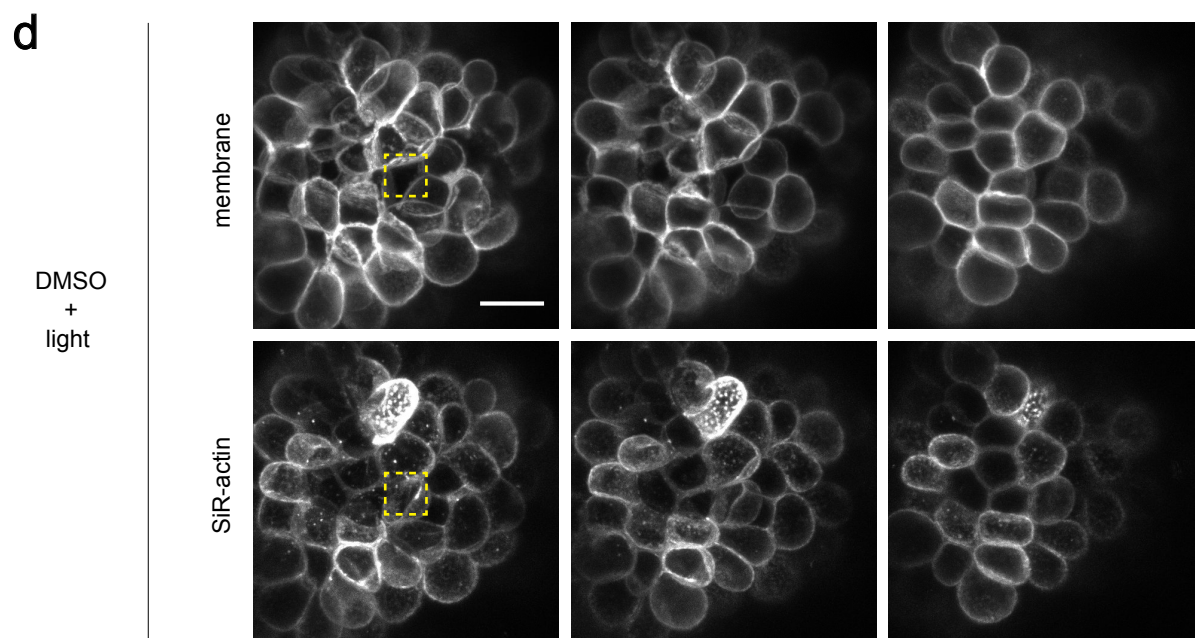
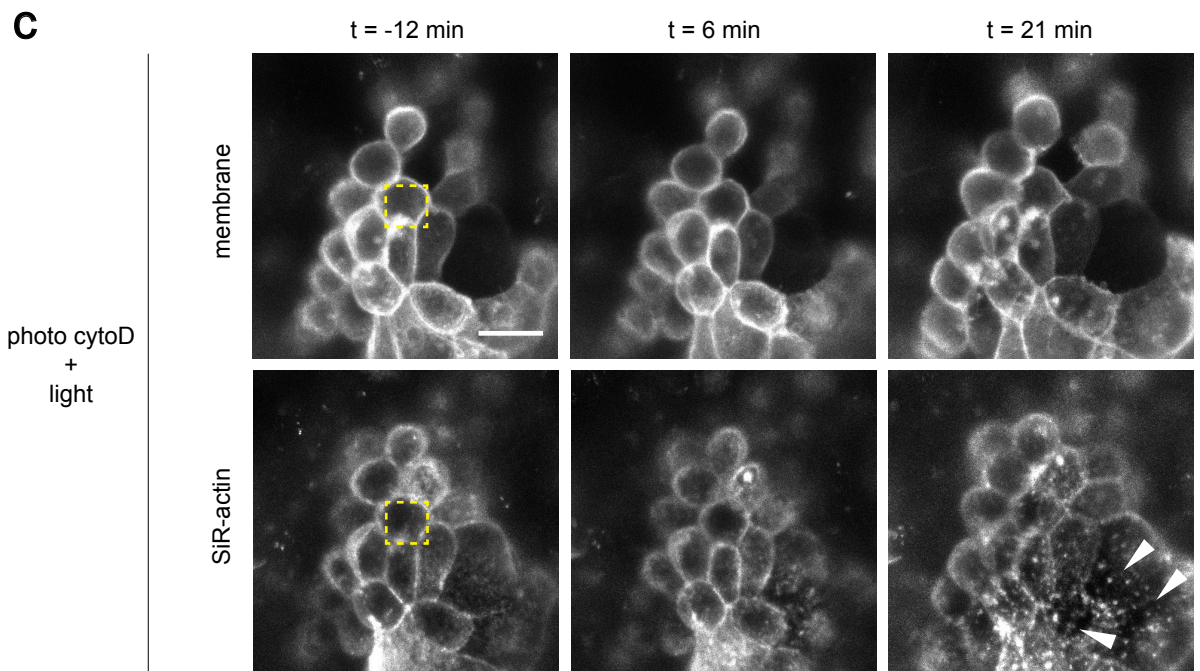
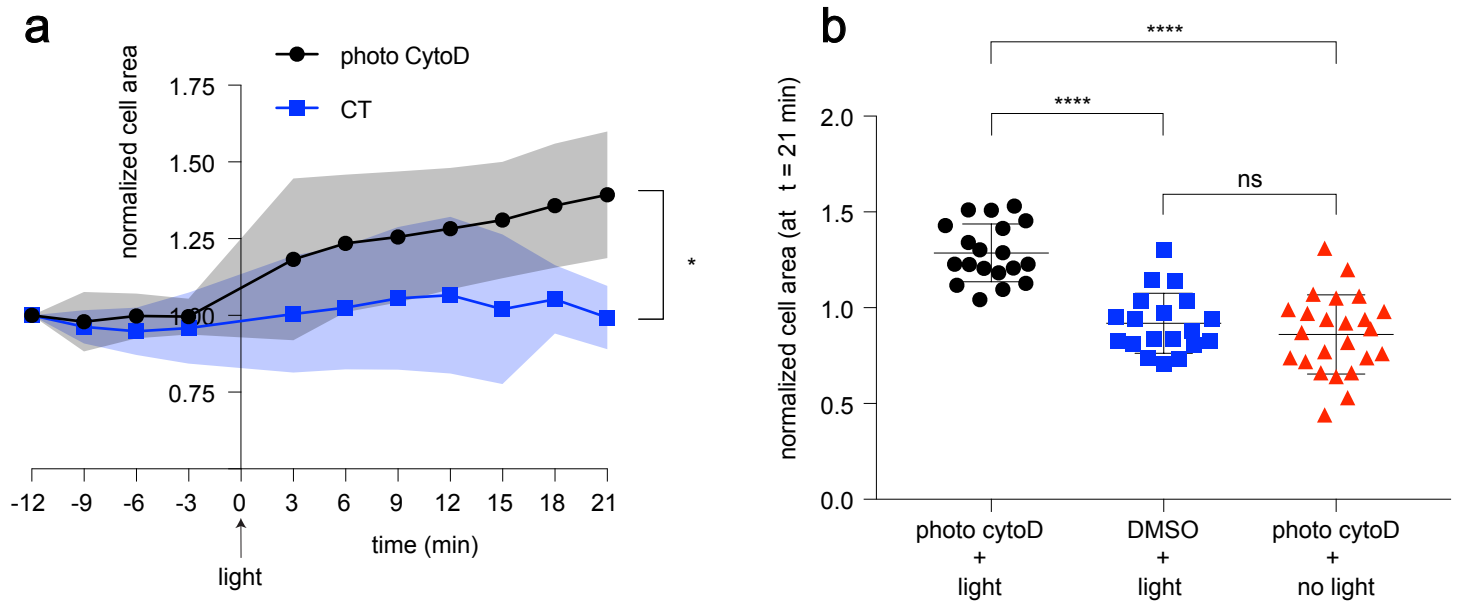
**f**



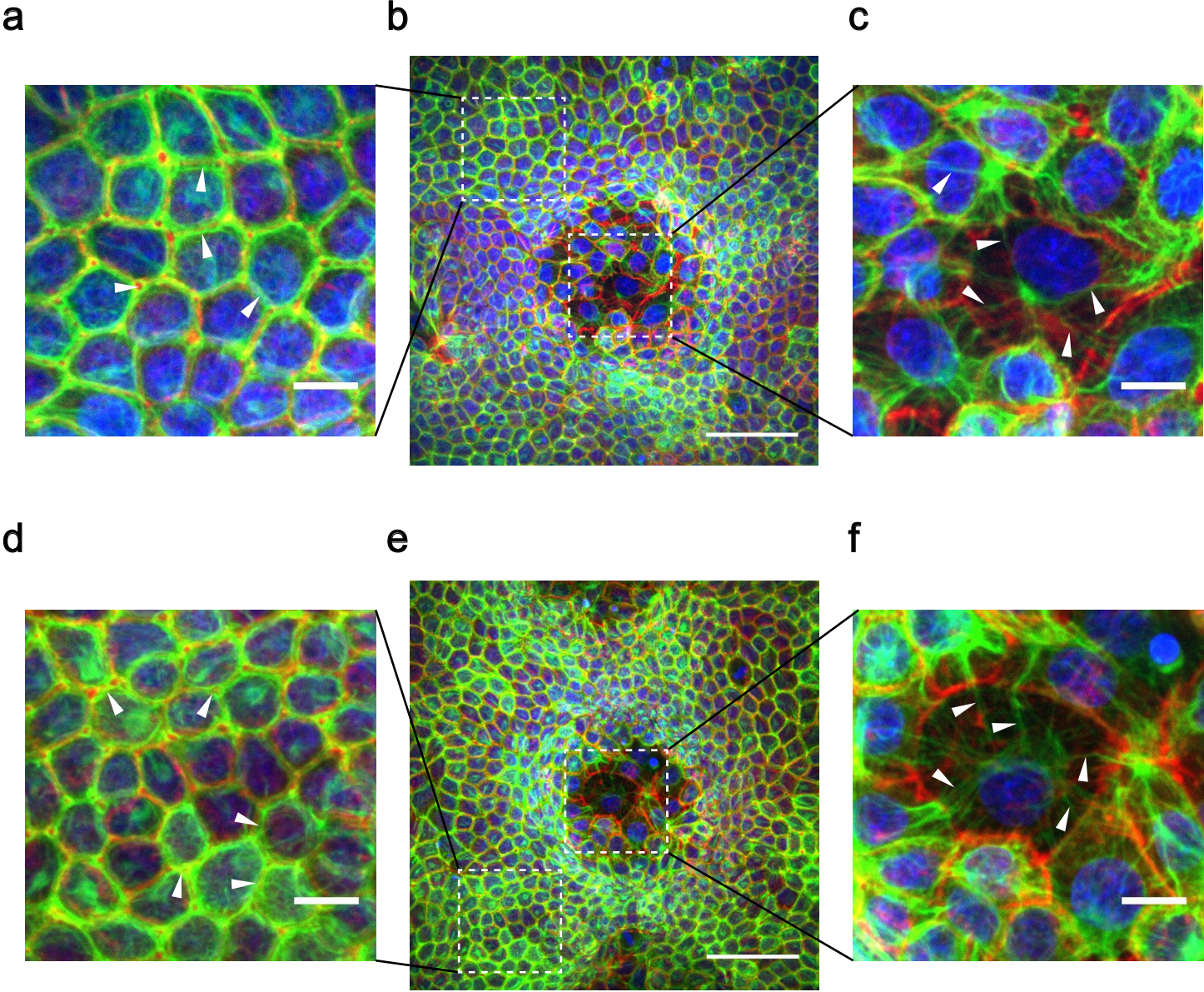
# Extended Data figure 7



# Extended Data figure 8



Extended Data figure 9



# Extended Data figure 10

